Effect of Direct Radiative Forcing of Asian Dust on the Meteorological Fields in East Asia during an Asian Dust Event Period

HYUN-JU AHN AND SOON-UNG PARK

School of Earth and Environmental Sciences, Seoul National University, Seoul, Korea

LIM-SEOK CHANG

Brookhaven National Laboratory, Upton, New York

(Manuscript received 17 May 2006, in final form 27 December 2006)

ABSTRACT

Coupled and noncoupled models in a grid of 60 × 60 km^2 in the eastern Asian domain have been employed to examine the effect of the direct radiative forcing of the Asian dust aerosol on meteorological fields for an intense Asian dust event observed in eastern Asia on 18–23 March 2002. The coupled model consists of the modified fifth-generation Pennsylvania State University–National Center for Atmospheric Research (NCAR) Mesoscale Model (MM5) with direct radiative forcing of the Asian dust aerosol through the NCAR Column Radiation Model and the Asian Dust Aerosol Model. The noncoupled model is MM5 without the direct radiative forcing of the Asian dust aerosol. The results indicate that the radiative cooling of the dust aerosol over the high-dust-concentration (HDC) region induces sinking motion and positive pressure perturbation near the surface, whereas the radiative warming of the aerosol near the top of the HDC layer induces rising motion and negative pressure perturbation, thereby enhancing the stable stratification in the dust layer. The induced positive pressure perturbation near the surface causes a dipole shape of the pressure perturbation field by forming a negative pressure perturbation toward the low pressure center downstream near the surface. This negative pressure perturbation is so deep and wide that the perturbation of the meteorological fields extends in the wide and deep regions away from the HDC region. The associated secondary circulation of this pressure perturbation reduces the low-level wind speed in the upstream HDC region but strengthens the downstream wind speed, resulting in reduction of dust emission in the upstream source region and downstream enhancement. Some of the dust aerosols lifted to the higher level by the synoptic rising motion are transported to the downstream direction more quickly with the upper-level strong wind, resulting in a bent-over shape of dust cloud in the downstream region with a maximum concentration near the surface and a secondary maximum in the upper level. The radiative flux convergence between these maximum dust layers produces a warm layer, thereby further enhancing the stable stratification.

1. Introduction

Dust storms are distinct features in many regions around the globe, including Australia, eastern Asia, western Africa, and South America (Schultz 1979; Prospero et al. 1979). In eastern Asia, Asian dust (*Hwangsa* in Korean), which is a typical example of mineral aerosol, frequently occurs in the sand desert, Gobi Desert, and loess plateau in northern China and Mongolia during the spring season (Park and In 2003; In and Park 2003; Park and Lee 2004). Some of the Asian dust events are reported to be transported to the western part of the United States across the Pacific Ocean (Husar et al. 2001; In and Park 2002). Husar et al. (2001) indicated that the dust clouds in eastern Asia increase the albedo over the cloudless ocean and land by up to 10%–20% and cause a whitish discoloration of the blue sky, suggesting the importance of the Asian dust on the atmospheric radiation balance.

Many researchers have conducted studies on the radiative effects of mineral aerosols (Miller and Tegen

Corresponding author address: Soon-Ung Park, School of Earth and Environmental Sciences, Seoul National University, Seoul 151-742, South Korea.
E-mail: supark@snu.ac.kr

DOI: 10.1175/JAM2551.1

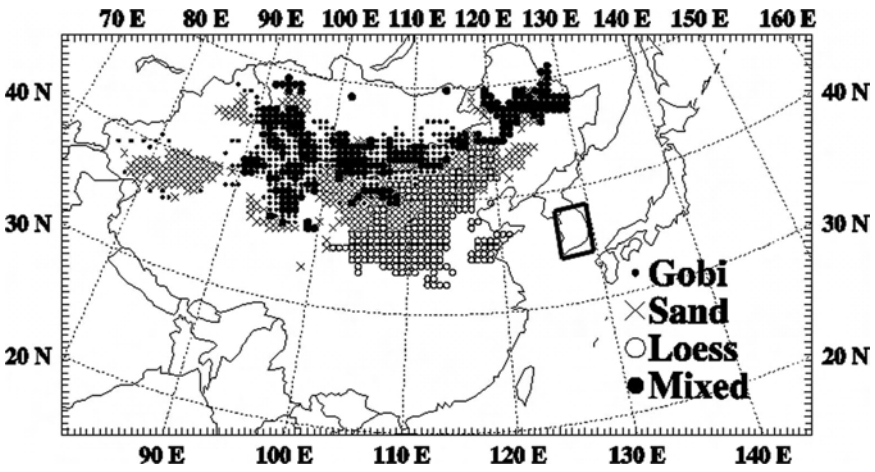

FIG. 1. Model domain with the indication of soil types in the Asian dust source region. The region of South Korea is given by a rectangle box.

1998; Tegen and Fung 1994, 1995; Tegen et al. 1996; Li et al. 1996; Andreas 1996) on the climate. On a global scale, the radiative forcing by dust generally causes a reduction in the atmospheric dust load (Perlwitz et al. 2001). Their experiments also showed that dust radiative forcing can lead to significant changes both in the soil dust cycle and the climate state. Miller et al. (2004) interpreted this reduction as an interaction between dust radiative forcing and the planetary boundary layer. Park et al. (2005) recently focused on the importance of Asian dust storms in the regional radiative forcing by using the National Center for Atmospheric Research (NCAR) Column Radiation Model (CRM) with the simulated spectral mass concentration distribution using the Asian Dust Aerosol Model (ADAM; Park and In 2003; Park and Lee 2004). However they used the outputs of the fifth-generation Pennsylvania State University–NCAR Mesoscale Model (MM5) meteorological field without the feedback mechanism with the Asian dust aerosol to estimate the direct radiative forcing of Asian dust. The domain-averaged direct radiative forcing of Asian dust in eastern Asia was estimated to be -6.6 W m^{-2} at the surface and -3.2 W m^{-2} at the top of the atmosphere. This implies that a significant impact of Asian dust aerosol relative to the greenhouse gas forcing on the meteorological fields is expected.

Therefore, we have developed a coupled model by combining the meteorological MM5 with ADAM through the NCAR CRM to examine the effect of Asian dust aerosol on the meteorological field. This coupled model has been implemented for an intense Asian dust event observed in Korea during 18–23 March 2002.

2. Model description

We define the coupled model as the combined model of the meteorological MM5 (Grell et al. 1994) with ADAM (Park and In 2003; Park and Lee 2004), considering the direct radiative effect of the dust aerosol through the CRM (Briegleb 1992).

a. Meteorological model

The meteorological model used in this study is MM5, defined in x, y, and σ coordinates (Grell et al. 1994; Dudhia et al. 1998). Physical processes including the CRM of the Community Climate Model, version 2, (CCM2) for radiation, the Kain–Fritsch scheme for convective parameterization, the Medium-Range Forecast Model (MRF) scheme for the planetary boundary layer processes, and the mixed phase of the moisture explicit scheme are used.

The model domain includes major source regions of Asian dust where soil types consist of sand, loess, gobi, and mixed soil (Fig. 1). The model has 120×65 grids having horizontal spacing of 60 km, with 20 vertical levels. The 6-hourly reanalyzed National Centers for Environmental Prediction data are used for the initial and boundary conditions for MM5. The modeling is performed with an integral time step of 3 min. The hourly outputs of the model are used for the analysis.

b. ADAM

The Asian Dust Aerosol Model developed by Park and In (2003) and modified by spectral dust emission flux in the source regions (Park and Lee 2004) has been used to calculate the temporal and spatial distributions

of the dust concentration in the model domain. We briefly describe this model. The model is based on statistically derived dust emission conditions (Table 1) in the specified dust source regions delineated by the World Meteorological Organization regular synoptic reporting data (Park and In 2003). The aerosol model includes physical processes such as three-dimensional advection, diffusion, and dry and wet depositions in the σ coordinate system (Westphal et al. 1987).

The governing equation is given by

$$\frac{\partial p_* C(r)}{\partial t} = -\frac{\partial p_* C(r) u}{\partial x} - \frac{\partial p_* C(r) v}{\partial y} - \frac{\partial}{\partial \sigma} C(r)(p_* \dot{\sigma} + g\rho V_f) + p_* \frac{\partial}{\partial x} K_h \rho \frac{\partial C(r)/\rho}{\partial x} + p_* \frac{\partial}{\partial y} K_h \rho \frac{\partial C(r)/\rho}{\partial y} + \frac{g^2}{p_*} \frac{\partial}{\partial x} K_z \rho^3 \frac{\partial C(r)/\rho}{\partial x} + p_* C_0 + p_* S,$$

where $C(r)$ is the concentration of spherical particles of radius r, u and v are the horizontal winds, V_f is the fall velocity (positive downward), $p_* = p_{\text{surf}} - p_{\text{top}}$, p_{surf} is the surface pressure, p_{top} is the model top pressure, ρ is the air density, g is the gravitational acceleration, K_h is the horizontal eddy diffusivity, K_z is the vertical eddy diffusivity, C_0 is the coagulation term, and S is the source and sink. Coagulation is not included in simulations because it is not an important process in the evolution of dust outbreaks (Westphal et al. 1987, 1988).

The second-order Bott scheme for the advection calculation is used to minimize the numerical diffusion term (Bott 1989). The planetary boundary layer scheme is used in MM5 with the nondimensional profile function of Businger et al. (1971).

The parameterizations of the Asian dust emission used in this study follow those of Park and In (2003) and Park and Lee (2004). In the Asian dust source region, soil types are composed of gobi, sand, loess, and mixed soil (Fig. 1). The composition of the soil texture at each source region is obtained from 37 soil samplings taken from each soil type in northern China (Park 2002).

The threshold wind speed and its corresponding threshold friction velocity (Westphal et al. 1988) are statistically determined using the synoptic reporting data in the source regions. Table 1 summarizes the conditions for the dust rise in the source regions (Park and In 2003).

TABLE 1. Conditions for the dust rise in the source region.

Source region	Threshold wind speed (m s^{-1})	Upper limit relative humidity (%)	Precipitation
Gobi	9.5	60	None
Sand	7.5	35	None
Loess	6.0	30	None
Mixed soil	9.2	45	None

The method for the estimation of dust emission amounts ranging from 0.2 to 74 μm in diameter is estimated as (Park and In 2003; Park and Lee 2004)

$$F_a = \left(1 - \sum_k f_k R_k\right) \alpha u_*^4 \quad \text{if} \quad u_* \geq u_{*t},$$

where F_a is the dust flux from the surface (g cm^{-2} s^{-1}), u_* is the friction velocity, u_{*t} is the threshold friction velocity, f_k is the fractional coverage of the k type of vegetation, R_k is the emission reduction factor due to the fractional coverage of vegetation (ranging from 0 for bare soil to 0.95 for broadleaf forest; In and Park 2002), and α is a constant (ranging from 4 to 5). The land use types classified by the U.S. Geological Survey vegetation categories are used in the source region. Twenty-four different types of land use in the horizontal resolution of 1 km are used for the determination of the vegetation coverage in each emission grid cell (Park and In 2003; Park and Lee 2004).

The spectral dust emission is estimated by the concept of the minimally and fully dispersed parent soil particle size distribution that depends on the erosiveness of the parent soil. The suspended particle size distribution $p_s(d)$ is a weighted average of minimally $p_m(d)$ and fully $p_f(d)$ dispersed parent particle size distribution (Lu and Shao 1999; Shao 2001) and is given by

$$p_s(d) = \gamma p_m(d) + (1 - \gamma) p_f(d),$$

where γ is the weighting factor, which is estimated by (Shao et al. 2002) as

$$\gamma = \exp[-k(u_* - u_{*t})^n] \quad \text{if} \quad u_* \geq u_{*t},$$

where $k = 27$ and $n = 3$ are constants and are determined empirically. For weak erosion ($u_* \approx u_{*t}$) γ approaches 1 and thereby the suspended particle size distribution is mainly controlled by the minimally dispersed parent soil particle size, whereas for strong erosion ($u_* \gg u_{*t}$) γ approaches 0 and thereby the fully

TABLE 2. Parameters for the lognormal distribution to construct minimally [$p_m(d)$] and fully [$p_f(d)$] dispersed particle size distributions for sand, loam, and silty clay using samples from northern China (Park and Lee 2004).

	Mode 1			Mode 2			Mode 3		
Sample	w_1	$\ln(D_1)$	σ_1	w_2	$\ln(D_2)$	σ_2	w_3	$\ln(D_3)$	σ_3
$p_m(d)$									
Sand	0.0329	4.3733	0.8590	0.9671	5.7689	0.2526			
Loam	0.0514	4.3565	0.0257	0.4931	5.4092	1.0000	0.4554	5.1674	0.3824
Silty clay	0.3000	4.4539	0.0236	0.0500	2.9319	1.0000	0.6500	4.5062	0.4473
$p_f(d)$									
Sand	0.0004	0.6931	1.0000	0.9960	5.6300	0.2542			
Loam	0.3100	4.6079	0.6141	0.5378	5.2050	0.2897	0.1522	7.0553	1.0000
Silty clay	0.0300	0.6931	1.0000	0.7700	1.8900	0.5000	0.2000	5.6930	1.0000

dispersed parent soil particle size distribution controls the suspended particle size distribution (Park and Lee 2004).

The minimally and fully dispersed particle size distribution for a given soil is expressed as the sum of several lognormal distributions (Gomes et al. 1990; Chatenet et al. 1996; Shao 2001; Park and Lee 2004):

$$p_{m,f}(d) = \frac{1}{d}\sum_{j=1}^{J}\frac{w_j}{\sqrt{2\pi}\sigma_j}\exp\left[-\frac{(\ln d - \ln D_j)^2}{2\sigma_j^2}\right],$$

where J is the number of modes, w_j is the weight for the jth mode of the particle size distribution, and D_j and σ_j are the parameters for the lognormal distribution of the jth mode. The nonlinear least squares fitting technique can be used to determine the parameters w_j, D_j, and σ_j from measured soil particle size distributions in the source regions (Park 2002; Park and Lee 2004). These parameters are given in Table 2.

The composition of the soil texture in Table 3 is approximated from 37 soil samplings taken in the gobi, sand, loess, and mixed soil regions in northern China (Park 2002).

The dry deposition flux is estimated from dry deposition velocity and airborne concentration near the surface (Seinfeld and Pandis 1998) with the dry deposition velocity of Wesely (1989) and Giorgi (1986).

The gravitational settling velocity v_f is computed by the Stokes law as

$$v_f = \frac{\rho_p g D_p^2}{18\mu},$$

where ρ_p is the density of the particle, D_p is the particle diameter, g is the gravitational acceleration, and μ is the dynamic viscosity of air. The particle density is assumed to be 2600 kg m^{-3} (Park and In 2003).

The wet deposition flux is estimated from the precipitation amount and the averaged dust concentration in the cloud water. Concentrations of dust for each in-cloud layer are calculated by taking into account the entrainment rates of air from the sides of cloud and top of the cloud that are determined by iteratively solving the mass conservation and the thermodynamic equations. Once the cloud volume is determined, the meteorological variables (temperature, pressure, liquid water content, and total water content) and dust concentrations are vertically averaged with the liquid water content weighting. The wet deposition amount of dust is determined by the precipitation amount and averaged dust concentration in the cloud water that is changed by the scavenging process. The detailed wet deposition process is given in In et al. (2003).

c. Optical model

The optical properties of dust aerosol [mass extinction efficiency, single-scattering albedo (SSA), and asymmetry parameter] depend on size and mineral components of dust. They are calculated by the Mie scattering code using each band, each size parameter, and observed refractive index. The refractive index used for calculating optical properties is obtained from average mineral components of soils obtained from 37 soil samples in the Asian dust source regions (Park et al. 2005). The dominant mineral components are quartz, feldspar, plagioclase, illite, kaolinite, and calcite in the order of the mass weight, and their refractive indices are given in Fig. 2.

TABLE 3. The composition of the soil texture in the source region.

	Soil texture		
Source region	Clay (%)	Loam (%)	Sand (%)
Gobi	10	40	50
Sand	4	6	90
Loess	20	70	10
Mixed soil	12	28	60

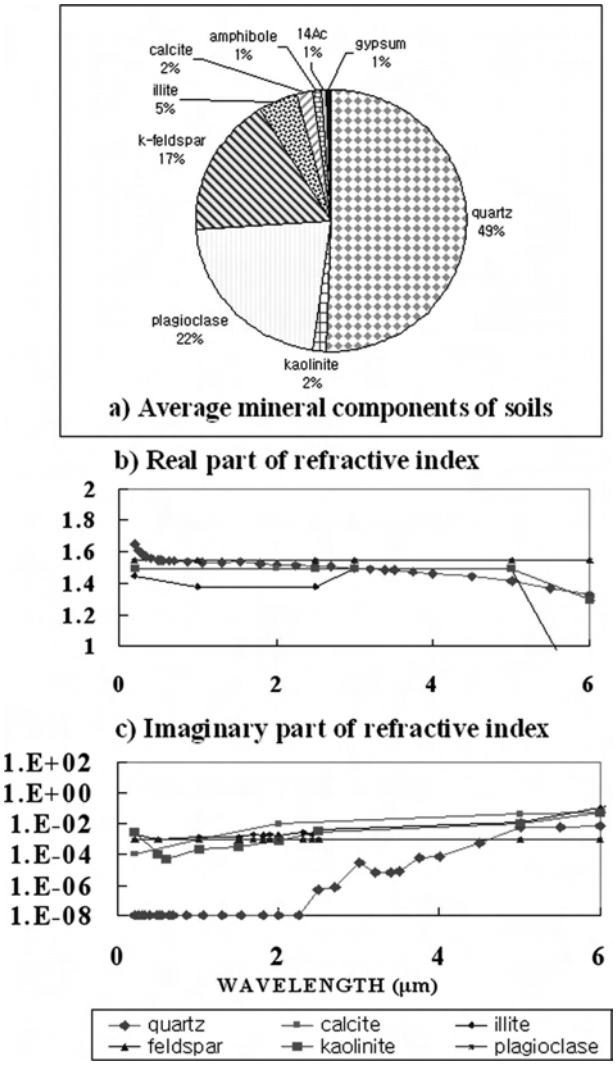

FIG. 2. (a) The average mineral components of soils in Asian dust source regions. (b) Real and (c) imaginary parts of refractive indices of various mineral components (Park et al. 2005, their Figs. 3 and 4). In (c), the *y*-axis scale indicates raising by a power of 10 (e.g., 1.E−08 = 10^{-8}).

d. Radiative transfer model

The CRM of CCM2 (Briegleb 1992) is used to estimate aerosol direct radiative forcing. The model uses a δ-Eddington approximation (Joseph et al. 1976) with 18 spectral bands [7 for ozone (O_3), 1 for the visible, 7 for water vapor (H_2O), and 3 for carbon dioxide (CO_2)] spanning the solar spectrum from 0.2 to 5.0 μm. It accounts for multiple scattering between model layers and includes gas absorption by O_3, molecular oxygen, CO_2, and H_2O and the effects of clouds. Vertical profiles of temperature, pressure, H_2O mixing ratio obtained from the MM5 simulation, and O_3 and CO_2 mixing ratio from the CRM model are used as the initial profiles for CRM.

The δ-Eddington method requires four optical properties to account for an aerosol: aerosol optical depth, SSA, asymmetry factor *g*, and the forward-scattering factor. We assume that the forward-scattering factor is equal to the square of the asymmetry parameter (Joseph et al. 1976; Chang 2005).

3. Model experiment

Two different model experiments have been conducted using ADAM and MM5 to examine the feedback effects of the direct radiative forcing of aerosols on meteorological fields. One is the "noncoupled model" experiment. ADAM is run to simulate the spatial and temporal variations of Asian dust aerosol concentration with the offline provision of the MM5 meteorological model. The estimated dust concentration is used to estimate the direct radiative forcing of the dust using the CRM. This direct radiative forcing does not affect the meteorological field.

The other is the "coupled model" experiment. The meteorological fields produced by MM5 at each integral time step are used to calculate the aerosol concentration by ADAM. The calculated aerosol concentration is used to estimate the optical properties using the optical model. The estimated optical properties are then fed back to the radiative scheme in MM5 for the next integral time step.

4. A case selection

A severe dust event has been observed in Korea for the period of 19–23 March 2002 with the maximum concentration exceeding 1000 μg m^{-3} at many monitoring sites over South Korea. Such intense dust storms occur more than 10 times per year in the source regions. However, the frequency in Korea is less than once per year. Park et al. (2005) have examined direct radiative forcing for the Asian dust aerosol and anthropogenic aerosols for this case. However, they have estimated direct radiative forcing of aerosols for the noncoupled model process with the offline provision of the meteorological fields. This Asian dust event has been selected for the case study.

Synoptic situations of the chosen case

The passage of frontal systems is one of the most effective mechanisms for a dust storm occurrence in northern China (Chung and Kim 1991; Chung and Park 1995; Chun et al. 2001). A surface low pressure center

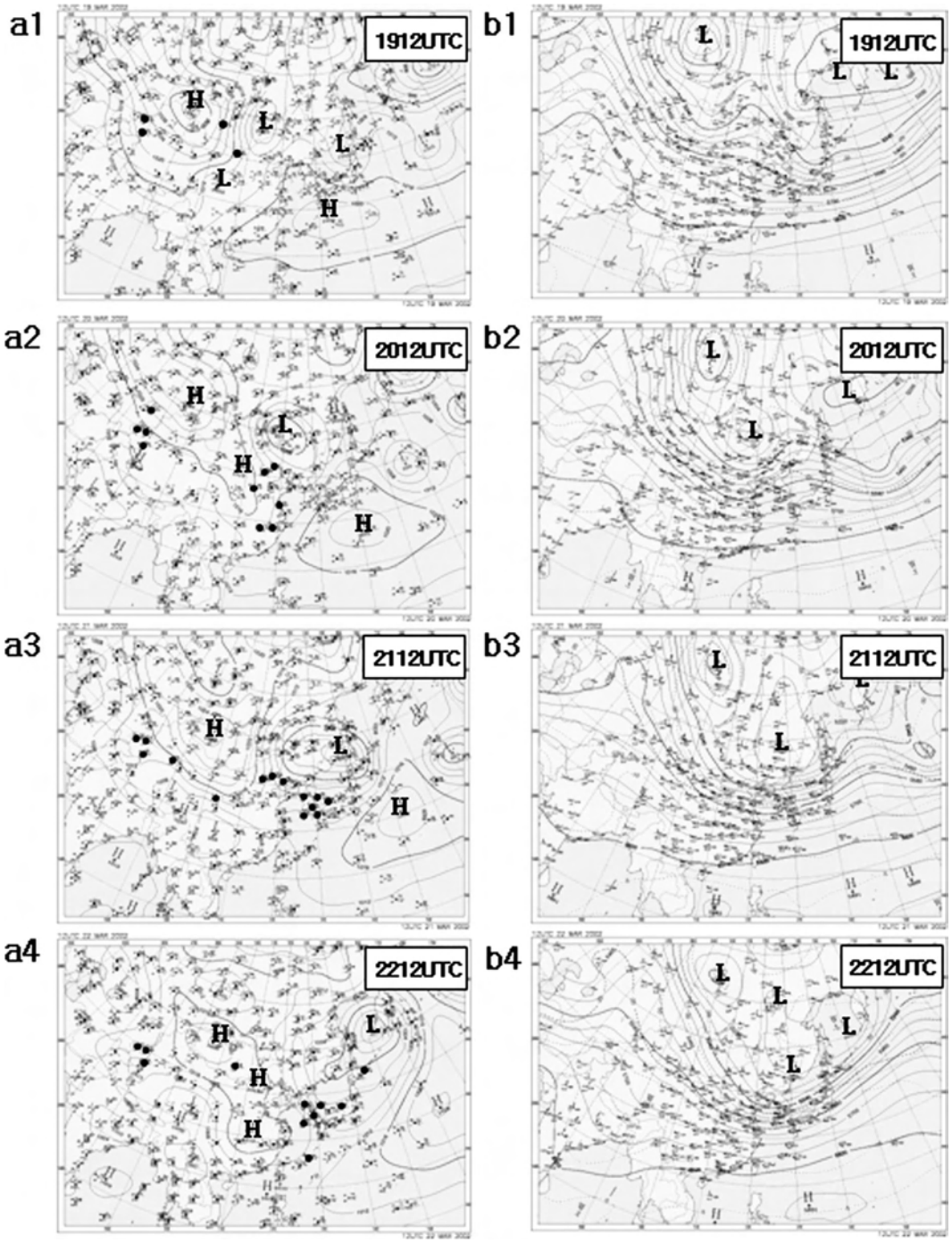

FIG. 3. Weather maps at 1200 UTC at (a) the surface and (b) 500 hPa from 19 to 22 Mar 2002 obtained from Korea Meteorological Administration. Dust-report stations are indicated by dots.

accompanied by a frontal system extending southwestward that separates the cold Siberian high pressure center to the northwest and the warm subtropical high to the southeast was located to the southeast of the Lake Baikal at 1200 UTC 19 March 2002 (Fig. 3a1). This surface frontal system was associated with the pressure trough at 500 hPa extending southwestward from the Lake Baikal. Behind the surface frontal system and in front of the Siberian high, dust rises have been reported. As the time progresses, the surface low pressure center moved slightly eastward whereas the accompanied frontal system moved fast southeastward as a re-

sult of the southeastward-expanding high pressure system behind it. A wide area of dust suspension in front of the expanding high pressure system behind the surface frontal zone has been reported over central eastern China at 1200 UTC 20 March (Fig. 3a2). The suspended dust has progressively moved southeastward (Fig. 3a3) over Korea and southern Japan as the high pressure centered over eastern Mongolia expands southeastward to merge with the subtropical high over the western Pacific while a well-developed surface low pressure system was located over Sakhalin. A wide dust-cloud area has been reported to the south of the surface low pressure system and the north of the surface high pressure ridge where the upper-level strong zonal flow has prevailed at the 500-hPa level at 1200 UTC 21 March 2002.

As the surface low pressure system progressively moves northeastward to Kamchatka the dust cloud also moves northeastward to northern Japan while the surface high pressure system centered at southern China extends northeastward (Fig. 3a4). Note that the dust-cloud region is located behind the surface pressure trough but in front of the upper-level pressure trough (Fig. 3b4) where the strong wind is prevailing at 1200 UTC 22 March 2002.

5. Results

a. Temporal variations of dust concentrations

Figure 4 shows the time series of modeled concentrations of particulate matter of diameter less than 10 μm (PM_{10}) averaged for the layer of below 100 m from the ground surface estimated by the coupled model and noncoupled model and observed PM_{10} concentration averaged over the South Korean region (Fig. 1). There are 127 monitoring sites scattered over South Korea. However, observed data at many sites are missing during the Asian dust period. Only 35 sites for which hourly observed PM_{10} concentration data are available are used for the average. The average has been calculated with the model values in grid cells that contain observation sites. Both models simulate relatively well the temporal variation of the PM_{10} concentration during the Asian dust period. The starting and ending time of simulated Asian dust are in good agreement with the observations over South Korea. However, the estimated PM_{10} concentration by the coupled model is slightly lower than that by the noncoupled model, suggesting that the impact of direct radiative forcing of aerosols on the dust concentration away from the source region is not very significant (Fig. 4a).

Figure 4b shows the simulated PM_{10} concentration averaged in the lower 100 m above the ground in the source region (35°–45°N, 105°–115°E) by the coupled and noncoupled model. The reduction of the dust concentration in the source region due to the direct radiative forcing of the dust aerosol is not large (about 10% at the time when the concentration is maximum), but the reduction of the vertical integrated concentration (Fig. 4c) is significant (about 30% of the maximum value). The maximum PM_{10} concentration at 1500 UTC 19 March in the source region (Fig. 4b) occurs about 39 h ahead of that in Korea (Fig. 4a).

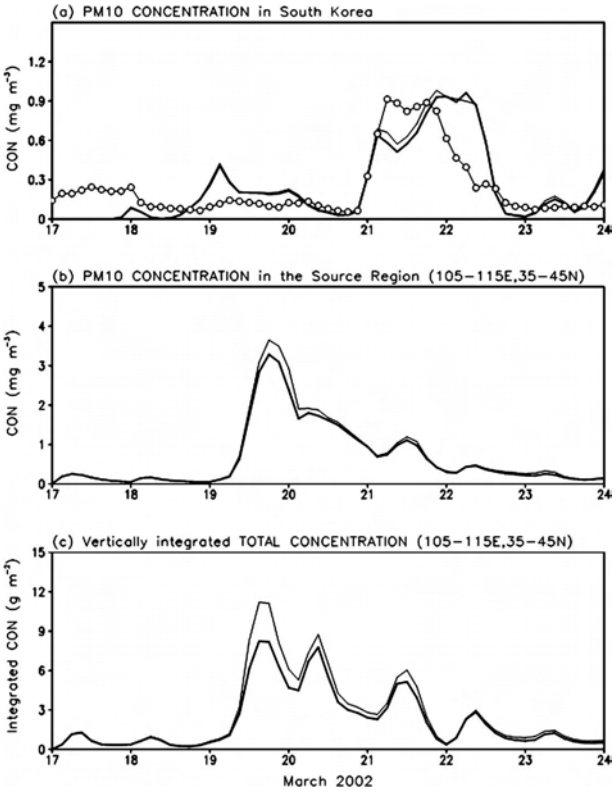

FIG. 4. Temporal variations of mean modeled PM_{10} concentrations (mg m^{-3}) by the coupled (thick line) and noncoupled (thin line) model averaged for the layer of below 100 m above the ground in (a) South Korea with the observed PM_{10} concentration (open circles) and (b) the source region (35°–45°N, 105°–115°E). (c) The vertically integrated modeled total concentration (g m^{-2}) in the source region.

b. Spatial distributions of dust emission and vertically integrated dust concentration

Figure 5 shows the temporal variation of the daily total dust emission amount (g m^{-2} day^{-1}) and daily averaged wind vector (m s^{-1}) at the surface layer simulated by the noncoupled model. Asian dust has occurred in wide regions along 40°N latitude line from 80° to 120°E in the Asian dust source regions (Fig. 1) in the strong surface westerlies, with a maximum emission rate of 20 g m^{-2} day^{-1} in the Taklamakan desert on 18

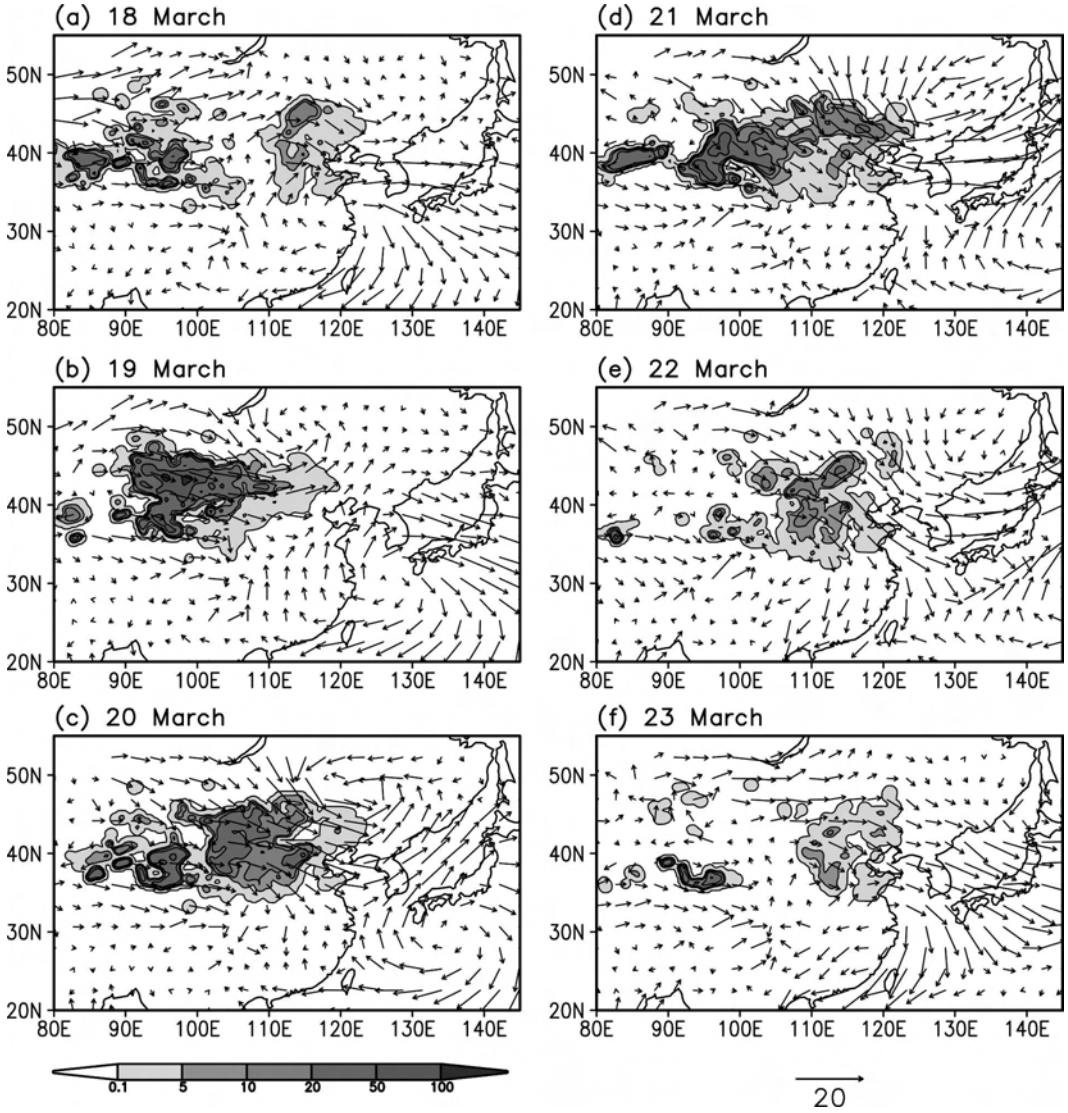

FIG. 5. Spatial distributions of model-simulated daily total emission amounts of dust (g m^{-2} day^{-1}) and daily averaged wind vector (m s^{-1}) at the surface layer by the noncoupled model for the period from 18 to 23 Mar 2002.

March 2002 (Fig. 5a). As the synoptic system gradually moves eastward (Fig. 3) the maximum dust emission zone (emission rate of more than 50 g m^{-2} day^{-1}) also moves eastward with intensification to be located in the region of 40°–45°N, 90°–105°E in the strong northwesterly flow behind the surface frontal system on 19 March (Fig. 5b). As the surface low pressure system accompanied with a strong cyclonic wind field keeps moving eastward, the maximum dust emission zone also moves eastward to the region of 37°–45°N, 100°–110°E, with a slightly reduced emission rate in the source region (Fig. 5c). Thereafter the low pressure system moves eastward progressively and the emission in the source region is reduced significantly on 23 March (Figs. 5e,f).

Very similar temporal and spatial distributions of the dust emission and the surface wind fields are obtained from the coupled model (not shown). However, the detailed patterns of the dust emission are changed as a result of the direct radiative forcing of the dust as seen in Fig. 6. The simulated dust emission by the coupled model is suppressed in the high-dust-emission regions, with the maximum reduction rate of 20 g m^{-2} day^{-1} (15% of the maximum emission rate) on 19 March when the emission rate is highest (Fig. 5b). This might be due to the radiative cooling of the dust at the surface, which, in turn, enhanced stabilization, and reduction of the surface wind lead to reduction of the emission rate (Miller et al. 2004). However, the dust emission downstream of the high-dust-emission region is

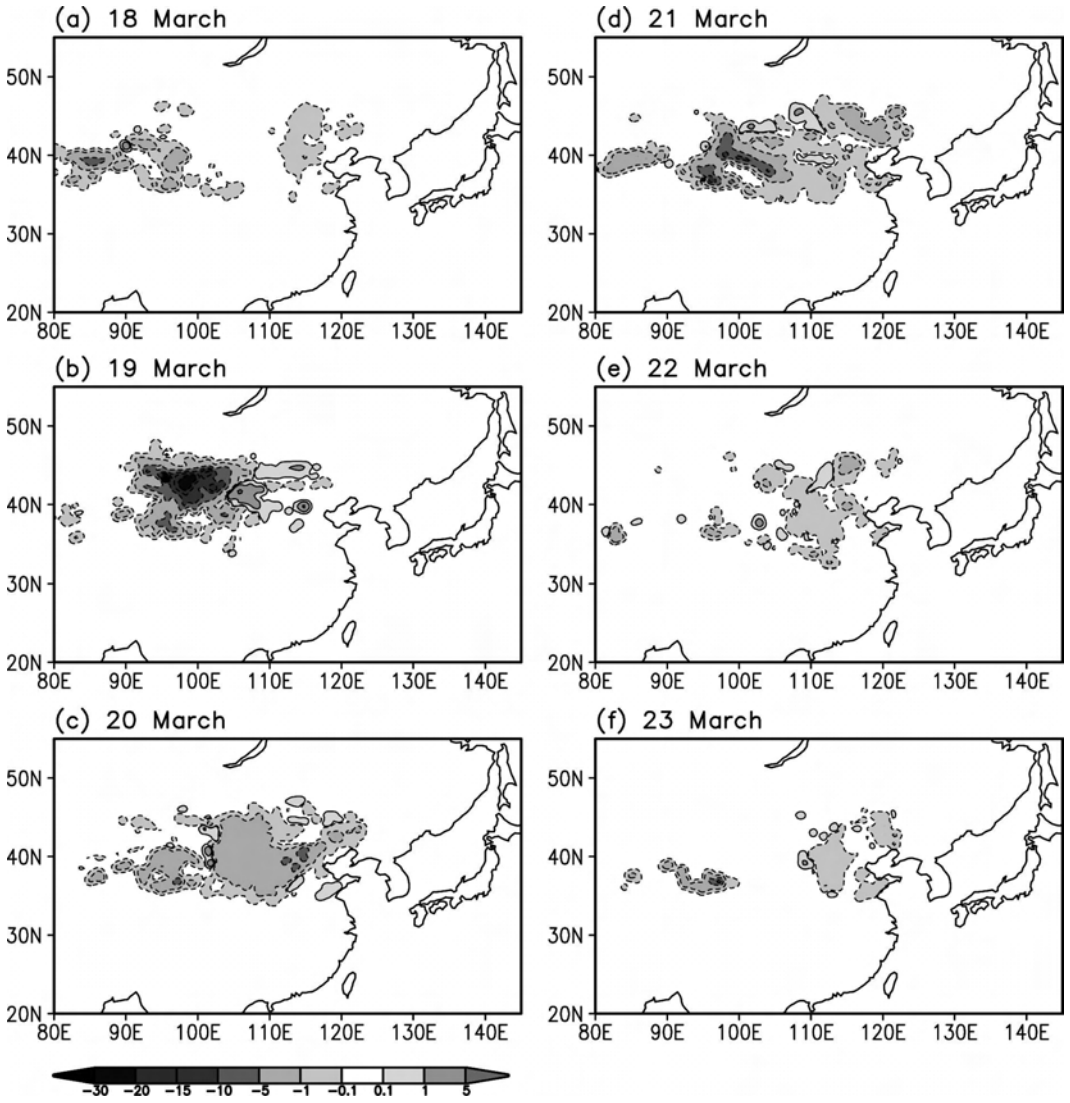

FIG. 6. Spatial distributions of the difference of daily total dust emission amount (g m^{-2} day^{-1}) simulated by the coupled and noncoupled models for the period from 18 to 23 Mar 2002. The areas enclosed by the dashed and solid curves show negative and positive values, respectively.

enhanced slightly (Fig. 6b) by the enhanced wind speed in association with the secondary circulation induced by the direct radiative forcing of the dust.

Figure 7 shows the spatial and temporal variations of daily averaged column dust concentration and the mean wind vector (m s^{-1}) at the 850-hPa level simulated by the noncoupled model.

On 18 March a high-dust-concentration zone simulated by the noncoupled model extends east-southeastward to the East China Sea covering central and eastern China. The edge of the dust cloud reaches the Kushu region in Japan (Fig. 7a). Dust emissions move eastward along the 850-hPa high wind zone to reach the eastern boundary of the analysis domain near Kushu on 19 March. The maximum column concentration of more than 3.2 g m^{-2} occurs in the maximum emission region (Fig. 5b) of 37°–42°N, 95°–105°E (Fig. 7b). On 20 March (Fig. 7c) the high-dust-concentration zone extends northeastward from central eastern China to northeastern China in association with the 850-hPa wind direction change from northwesterlies to southwesterlies over northeastern China. It then extends farther eastward over central-eastern China, Korea, and the East Sea (Fig. 7d) as the low pressure system moves southeastward accompanied with strong winds at 850 hPa. Thereafter, it continuously moves east-southeastward with decreasing intensity along the 850-hPa maximum wind zone (Figs. 7e,f).

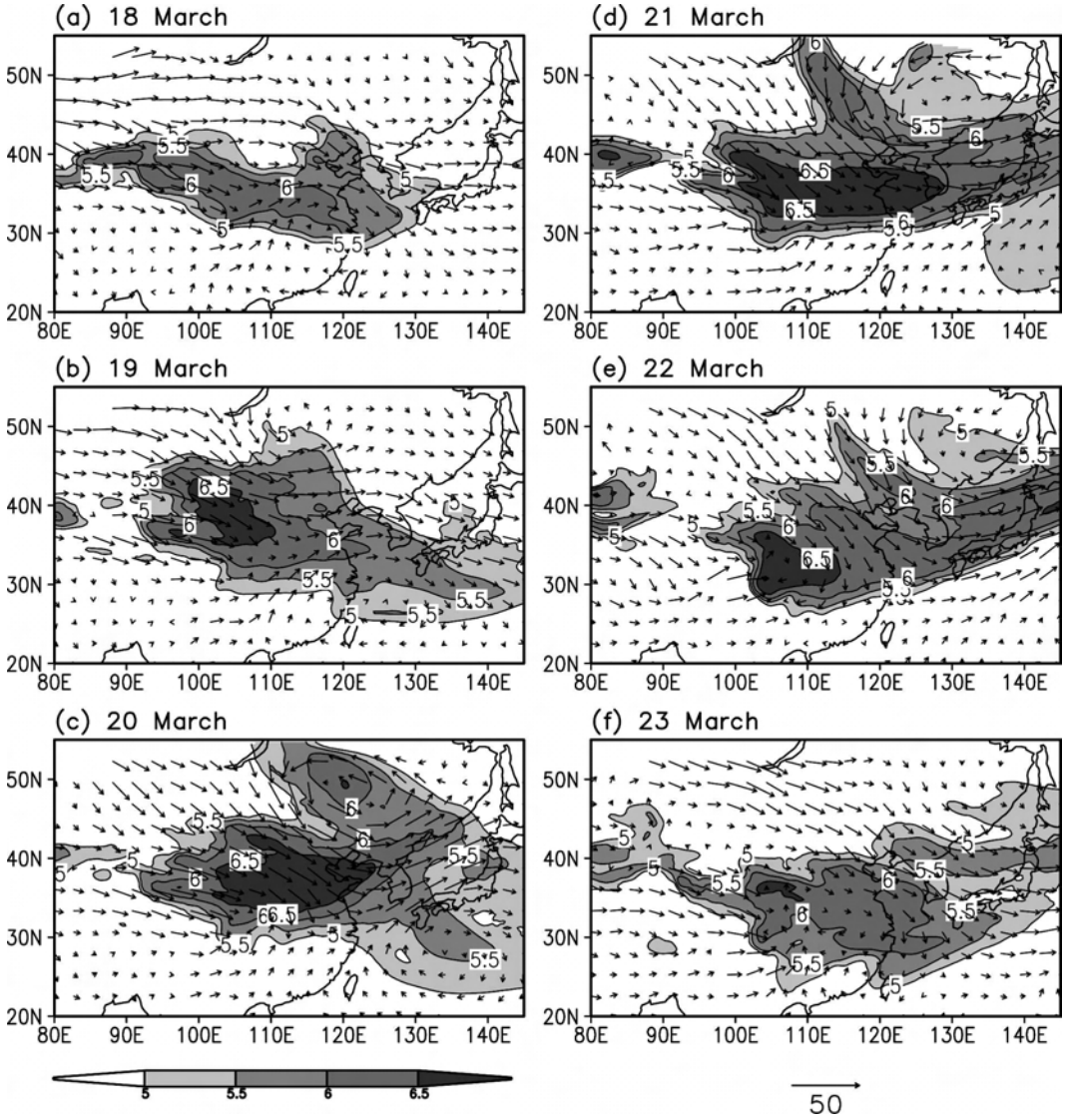

FIG. 7. Spatial distributions of the daily averaged vertically integrated dust concentration (μg m^{-2}) expressed in common logarithm and daily averaged wind vector (m s^{-1}) at 850 hPa simulated by the noncoupled model for the period from 18 to 23 Mar 2002.

The temporal and spatial variations of the column-integrated daily mean dust concentration simulated by the coupled model show very similar patterns (not shown) except for the reduced dust concentration in the high-dust-concentration region simulated by the noncoupled model.

The spatial distribution of the column-integrated dust concentration difference between two models (Fig. 8) clearly indicates that the coupled model produces less dust concentration than does the noncoupled model. The maximum reduction region of the dust concentration coincides with the maximum dust concentration regions simulated by the noncoupled model (Fig. 7). However, the maximum percentage reduction regions of the column-integrated dust concentration (Fig. 9) do not coincide with the regions of the maximum reduced dust concentration estimated by the coupled model (Fig. 8). The percentage reduction of the column-integrated dust concentration ΔC_p is defined as $\Delta C_p = 100(C_c - C_{\rm nc})/C_{\rm nc}$, where $C_{\rm nc}$ is the column-integrated dust concentration estimated by the noncoupled model and C_c is that by the coupled model. The maximum ΔC_p occurs in the flow-diverging areas at 850 hPa (Fig. 7) around the regions of maximum reduced dust concentration in Fig. 8, whereas in the far downstream region where the flow is converging large negative ΔC_p values occur. This suggests that the coupled model tends to spread the dust concentration more widely to-

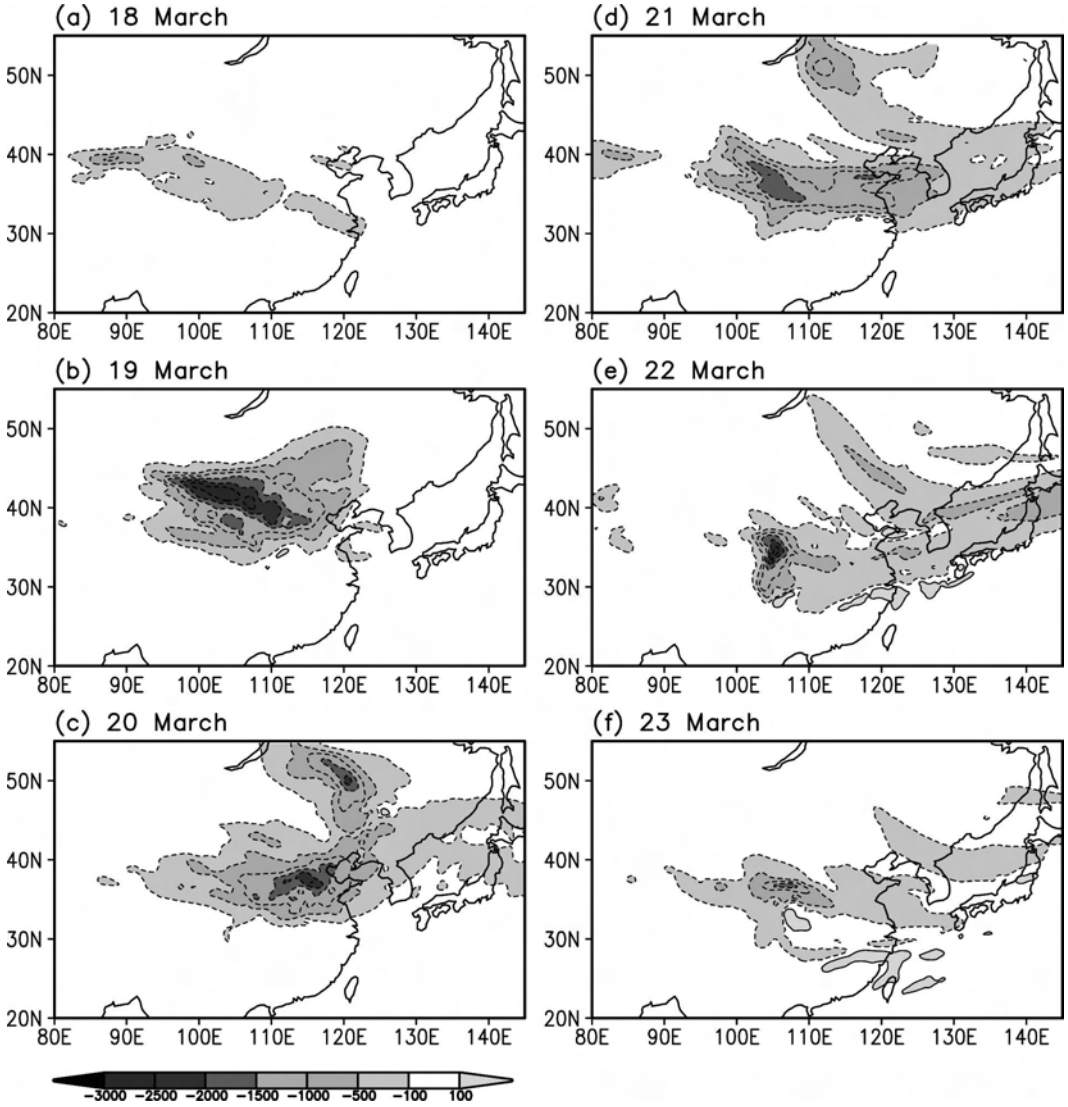

FIG. 8. Spatial distributions of the daily averaged column-integrated concentration difference (mg m^{-2}) simulated by the coupled and noncoupled models for the period from 18 to 23 Mar 2002. The area enclosed by the dotted curve indicates where the dust concentration simulated by the noncoupled model is higher than that simulated by the coupled model.

ward the downstream region by reducing dust concentration in the high-concentration region and enhancing dust concentration in the low-concentration region.

c. Estimation of aerosol direct radiative forcing

To estimate the direct radiative forcing due to Asian dust aerosols, the NCAR CRM (Kiehl et al. 1998; Briegleb 1992) is used with the simulated Asian dust concentration by the noncoupled model and the coupled model.

Vertical profiles of temperature, pressure, and H_2O mixing ratio obtained from the MM5 simulation and those of O_3 and CO_2 mixing ratios from the CRM are used as the initial profiles for the CRM. The aerosol direct radiative forcing is obtained as the difference in shortwave net radiative fluxes between CRM simulations with and without aerosol mass loadings simulated by ADAM.

Figure 10 shows the spatial distribution of 24-h mean direct radiative forcing at the surface (SRF) due to Asian dust aerosol simulated by the noncoupled model (Fig. 7). The spatial distribution pattern of SRF follows that of the Asian dust concentration simulated by the noncoupled model with a maximum value of more than –80 W m^{-2} on 19 March (Fig. 10b) in the high-dust-concentration region around 100°E and 42°N. This

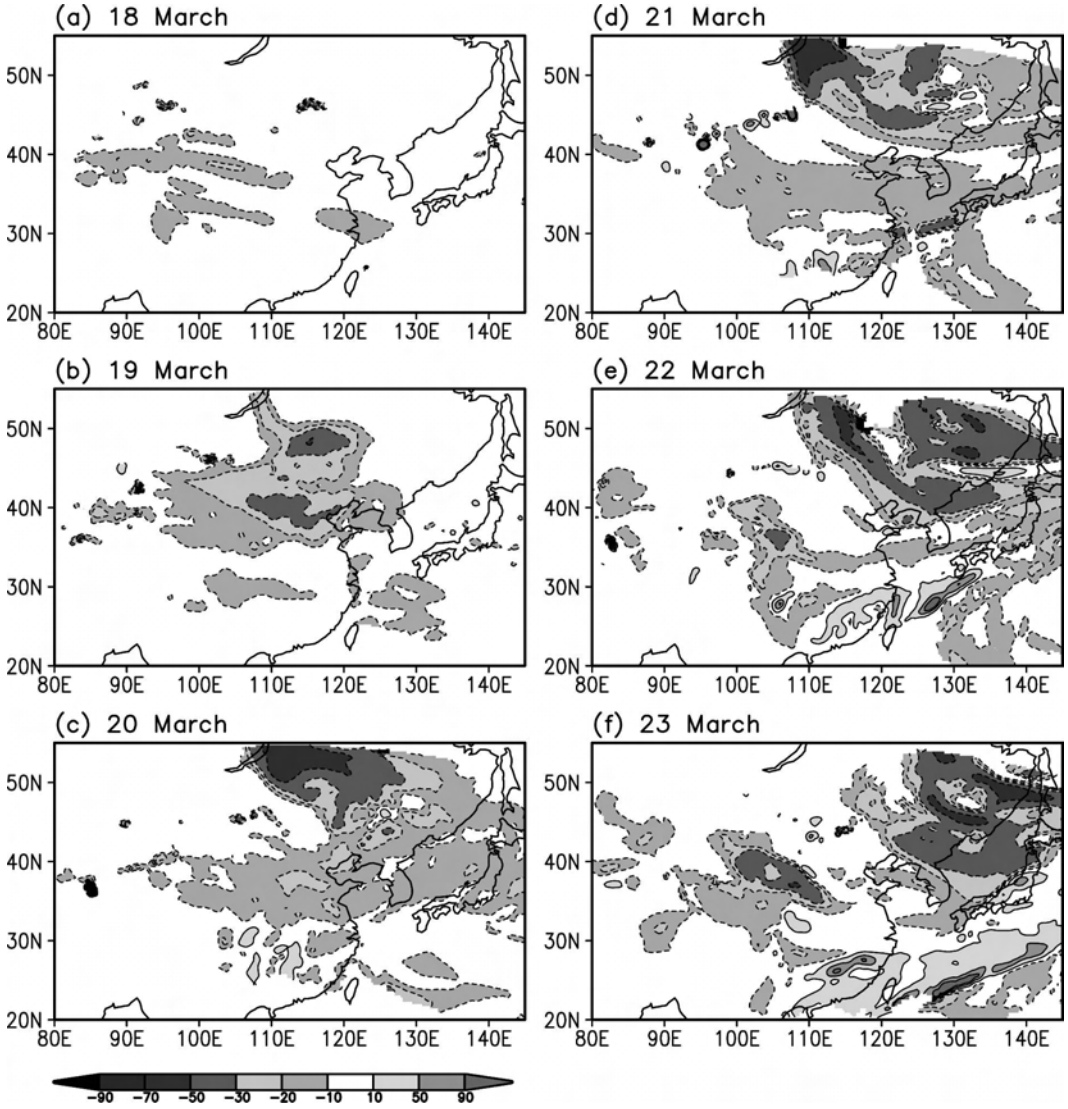

FIG. 9. As in Fig. 8, but for the percentage difference (%).

high-negative-SRF region moves continuously southeastward, reaching over the Yellow Sea on 21 March (Fig. 10d) and the East Sea on 22 March (Fig. 10e). Thereafter, it is weakened significantly on 23 March (Fig. 10f).

The SRF values calculated by the coupled model (not shown) are slightly smaller negative values (relative difference is positive) than those values calculated by the noncoupled model in the high-dust-concentration regions because of the reduction of dust concentration (Fig. 8), whereas away from and around the high-dust-concentration regions, especially in the downstream regions, the negative radiative forcing calculated by the coupled model is larger than that of the noncoupled model in the wide downstream regions even though its spatial distribution is somewhat disorganized (Fig. 11). This scattered pattern is associated with the changes of aerosol concentration and the cloud amount (Fig. 12) induced by the direct radiative forcing of the dust aerosol. The change of cloud amount (Fig. 12) mainly occurs in the lower latitudes and the synoptic low pressure systems. However, the cloud amount change is less than 0.2.

d. Impacts of the direct radiative forcing of the Asian dust aerosol on meteorological fields

1) TEMPERATURE FIELD

The impact of the direct radiative forcing of the aerosol on the temperature may be obtained from the tem-

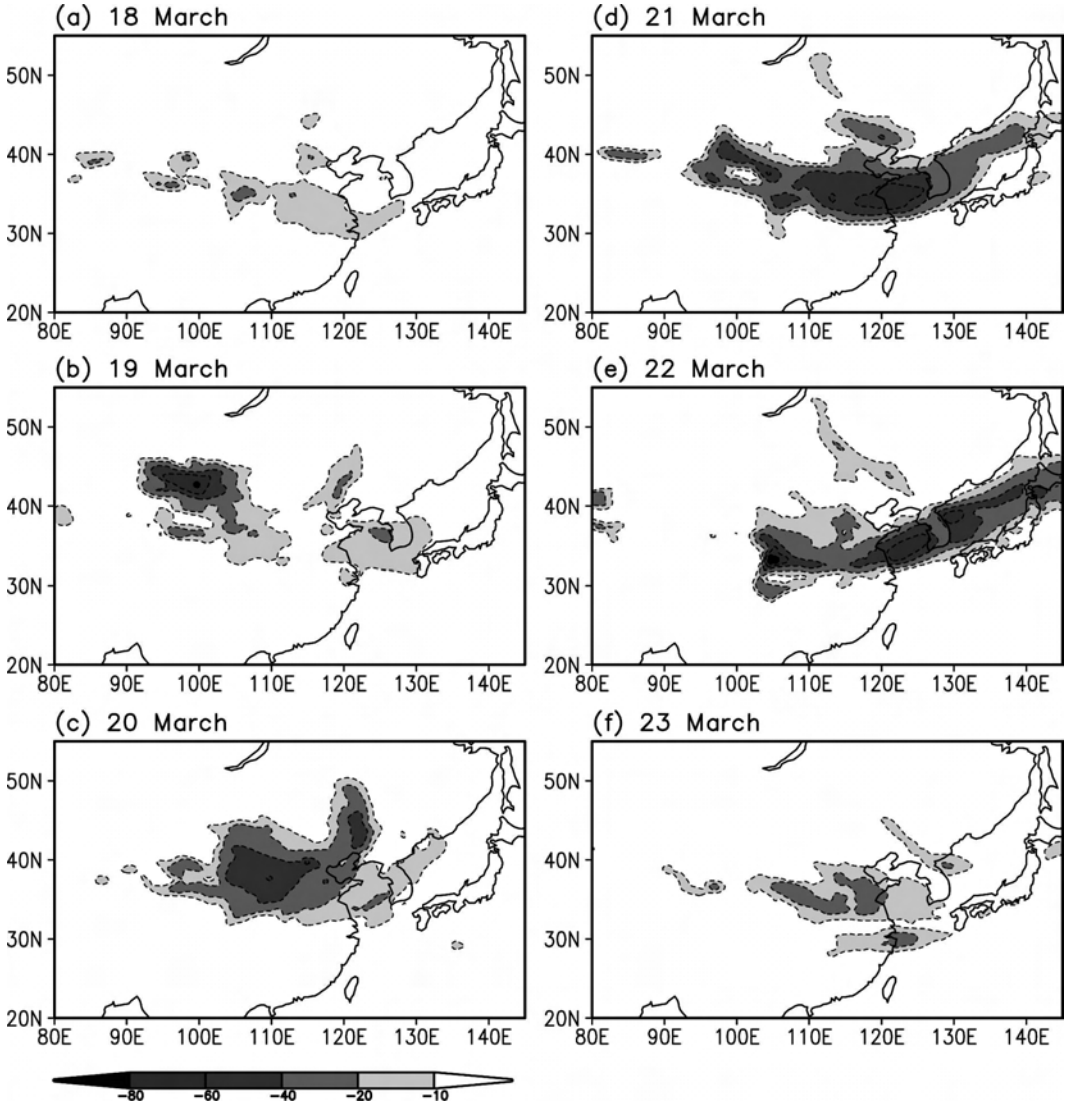

FIG. 10. Evolutional features of the spatial distribution of daily averaged direct radiative forcing (W m^{-2}) at the surface due to Asian dust aerosol simulated by the noncoupled model from 18 to 23 Mar 2002.

perature difference between the model results with (coupled model) and without (noncoupled model) the direct radiative forcing of the aerosol. The spatial and temporal variations of the 24-h mean surface temperature affected by the Asian dust aerosol (Fig. 13) follow those of the vertically integrated dust concentration simulated by the noncoupled model (Fig. 7) with lower surface temperature over the high-dust-concentration region because of direct radiative cooling of the aerosol at the surface (Fig. 10). The maximum decrease of more than 1.5°C of the 24-h mean surface temperature difference occurs on 21 March (Fig. 13d) over the central eastern part of China where the vertically integrated dust concentration exceeds 3×10^6 μg m^{-2}. As the dust clouds move eastward away from the source regions, the cool air affected by the Asian dust aerosol spreads widely toward the downstream regions covering all of eastern China and Korea and produces a slight temperature difference at the downstream edge of the cool air over northern China and Japan (Fig. 13).

The cool air produced by the aerosol radiative cooling barely extends up to 850 hPa on 18 March in the dust-rise regions, probably because of the shallow dust layer in the source regions (Fig. 14a). However, from 19 March when the dust concentration is high, the cool air caused by the aerosol radiative forcing extends to the 850-hPa level with the slight enhanced warm air in the wide downstream regions of the dust layer (Fig. 14). The cooling effect of aerosol on the temperature almost disappears in the 500-hPa level, but slightly warmed air

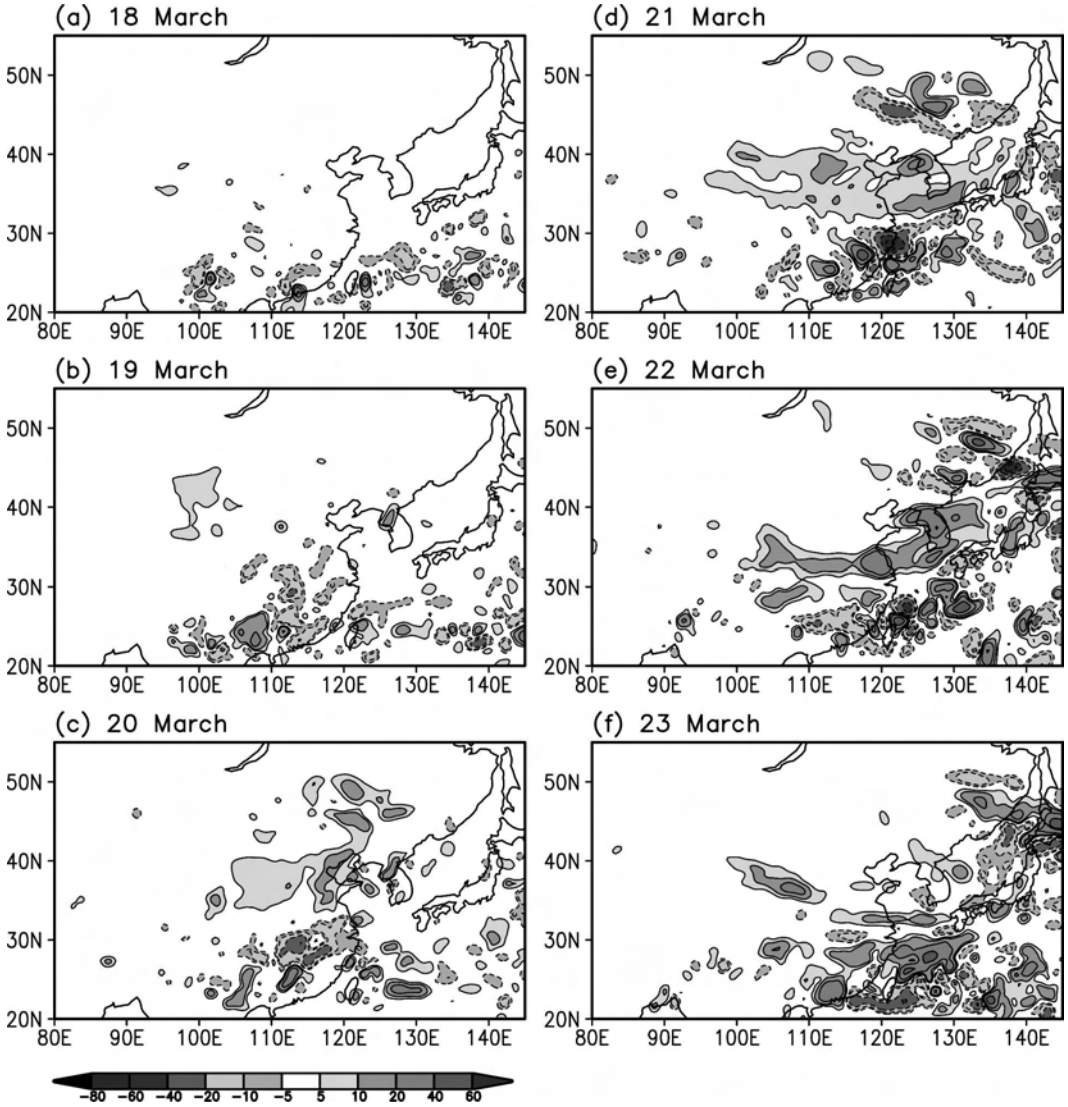

FIG. 11. As in Fig. 10, but for the difference of SRF (W m^{-2}) simulated by two models. The positive and negative values are respectively enclosed by the solid and dashed curves.

prevails over Korea and Japan in the downstream region of high dust concentration (not shown).

2) PRESSURE FIELD

The impact of the direct radiative forcing of the Asian dust aerosol on the pressure field is shown in Figs. 15 and 16 at the surface and 850 hPa, respectively. The spatial and temporal variations of the pressure difference are obtained by subtracting the pressure field simulated by the noncoupled model (without the aerosol effect) from that simulated by the coupled model (with the aerosol effect).

The radiative cooling due to the aerosol near the surface (Fig. 10a) over the high-dust-concentration region (Fig. 7a) produces a positive pressure perturbation with the maximum value of less than 0.4 hPa near the surface on 18 March (Fig. 15a). As the dust layer moves southeastward along the prevailing northwesterlies with the increased dust concentration over the source region of 35°–45°N, 100°–110°E on 19 March (Fig. 7b), the positive pressure-perturbation zone in association with the radiative cooling of the aerosol near the surface (Fig. 10b) is also extended southeastward with increased intensity (Fig. 15b). In the mean time a negative pressure-perturbation zone is formed to the north of the maximum positive pressure difference region. On 20 March the perturbed pressure field due to direct radiative effect of the aerosol (Fig. 15c) has formed a

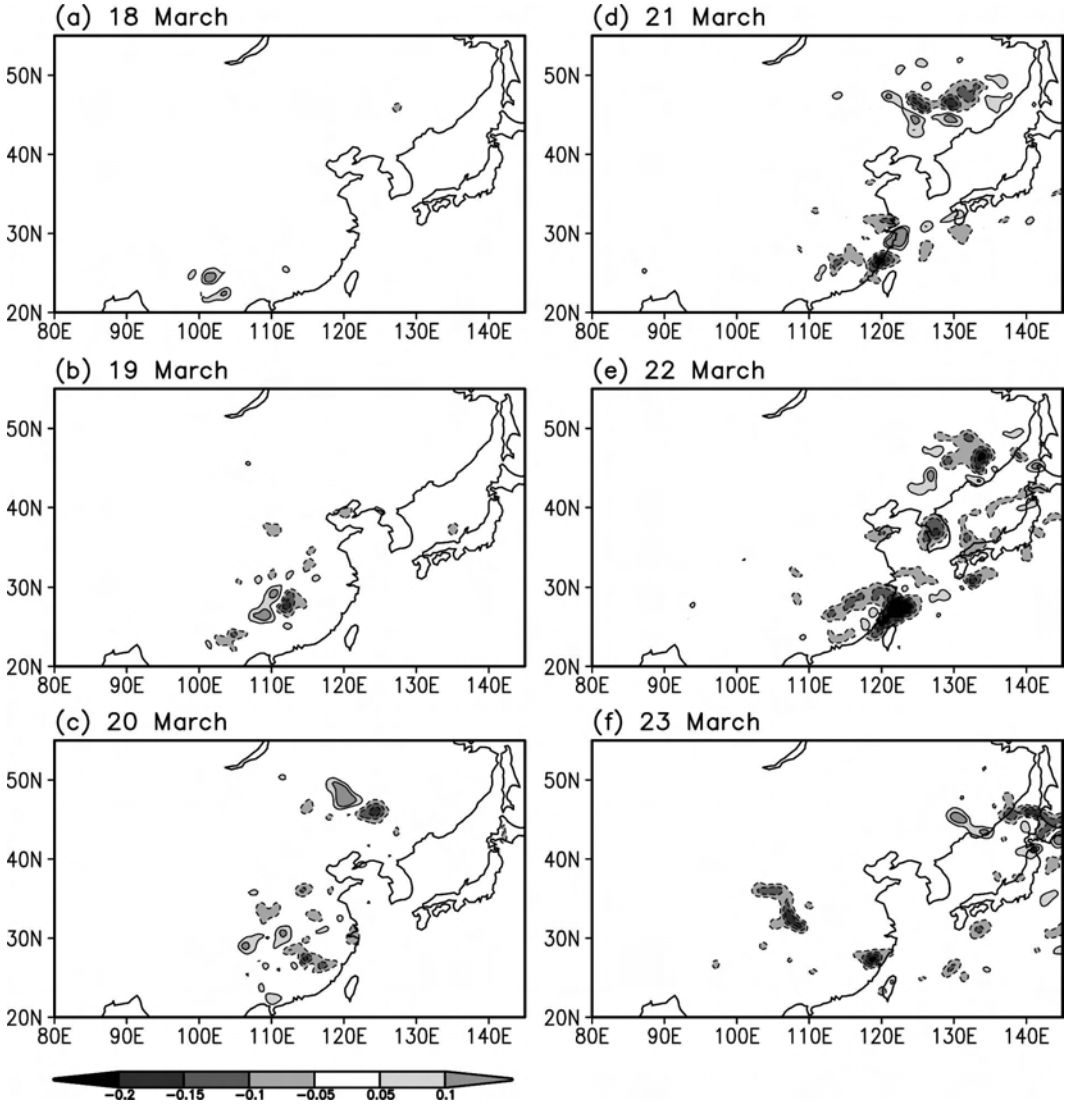

FIG. 12. As in Fig. 11, but for the difference of cloud amount simulated by the coupled model and noncoupled model.

distinctive dipole structure near the surface with a negative maximum pressure perturbation of more than 0.8 hPa at around 120°E and 47°N and a positive maximum pressure perturbation of more than 0.6 hPa at around 110°E and 35°N where the maximum radiative cooling (Fig. 10c) occurs because of the maximum aerosol concentration (Fig. 7c). This dipole structure of the perturbed pressure field has progressively moved southeastward (Figs. 15d,e,f) having a maximum intensity on 21 March (Fig. 15d) when the radiative cooling reaches its maximum (Fig. 10d) because of the maximum dust concentration (Fig. 7d).

Figure 16 shows the spatial distribution of the perturbed pressure due to the direct radiative effect of the Asian dust aerosol at $\sigma = 0.825$ (≅850 hPa). The dipole structure of the pressure-perturbation field is not clear at this level. The region of the positive pressure perturbation over the high-aerosol-concentration region (Fig. 7) is reduced dramatically whereas the induced negative pressure perturbation remains, suggesting a thin Asian dust layer in the positive pressure-perturbation region. At the $\sigma = 0.45$ (≅500 hPa) level the positive pressure-perturbation region disappears whereas the negative pressure perturbation is expanded in the downstream region of the Asian dust source region with reduced intensity (not shown). This clearly indicates that the effect of direct radiative forcing of the Asian dust aerosol on the pressure field is mainly confined in the lower shallow layer within 850 hPa over the high pressure system with a positive pressure perturba-

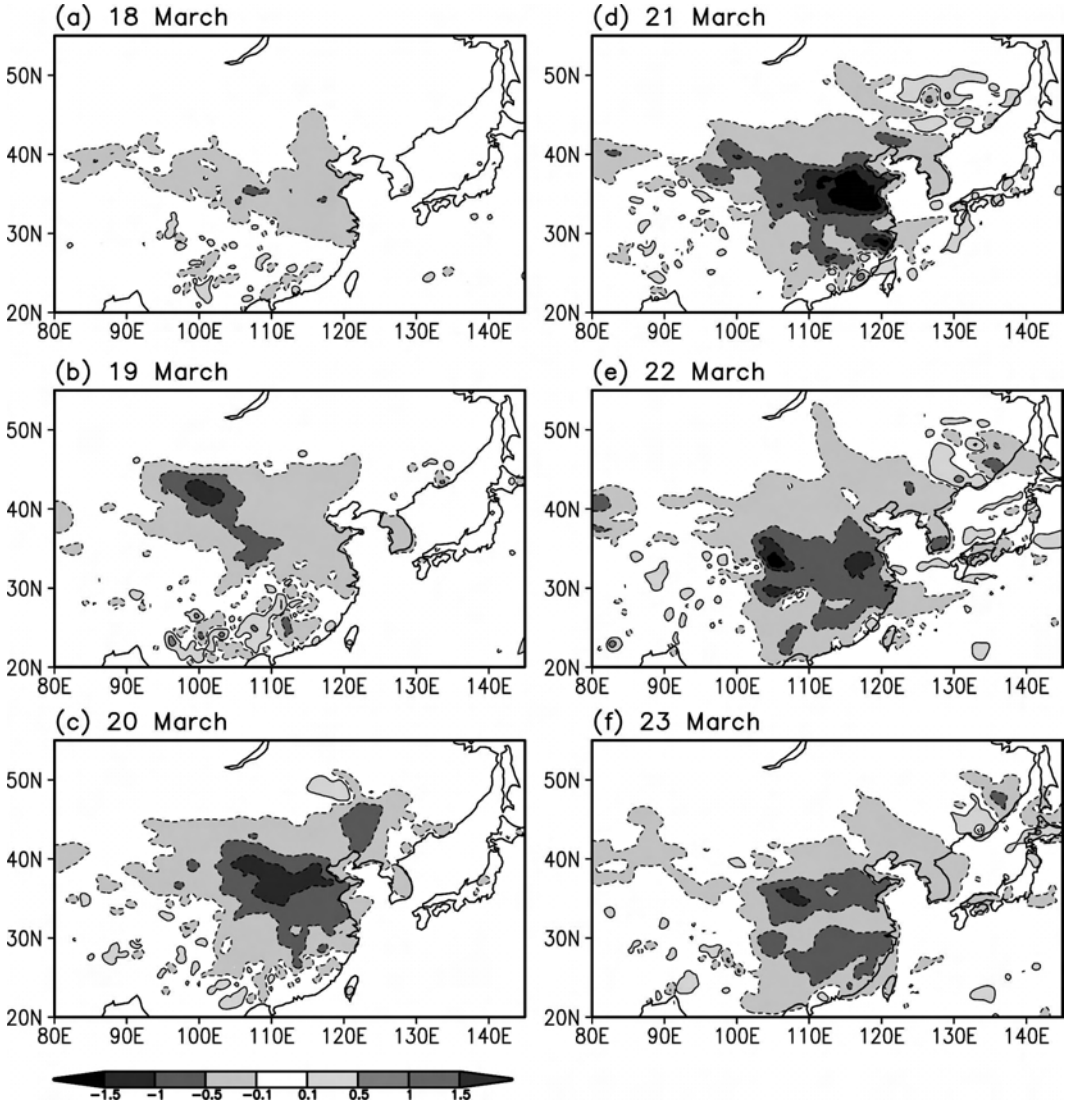

FIG. 13. Spatial distributions of the difference of temperature (°C) simulated by two models at the surface. The negative and the positive values are respectively enclosed by the dashed and solid curves.

tion, whereas over the low pressure system the effect is felt through a deeper layer to produce a negative pressure perturbation in the downstream region.

3) WIND FIELD

The effect of the direct radiative forcing of the Asian dust aerosol on the wind field is estimated from the wind vector difference between the model results with (coupled model) and without (noncoupled model) the direct radiative forcing of the aerosol.

The perturbed wind vectors affected by the effect of Asian dust aerosol at the $\sigma = 0.9975$ (near surface) and 0.825 (≅850 hPa) levels are also given in Figs. 15 and 16, respectively. The perturbed wind vectors are well correlated with the pressure perturbations with anticyclonic circulations around the positive pressure-perturbation regions and cyclonic circulations around the negative pressure-perturbation regions in all levels. At the surface (Fig. 15) most of the largest wind anomalies are down the pressure gradient rather than parallel to the anomaly isobars.

The maximum perturbed wind occurs on 21 March as northwesterlies over the Yellow Sea between the dipole structure of the pressure perturbation whose intensity reaches its maximum at the surface level (Fig. 15d). Higher up at the $\sigma = 0.825$ (≅850 hPa) level (Fig. 16) the maximum perturbed wind occurs to the north of the negative pressure-perturbation region as easterlies over

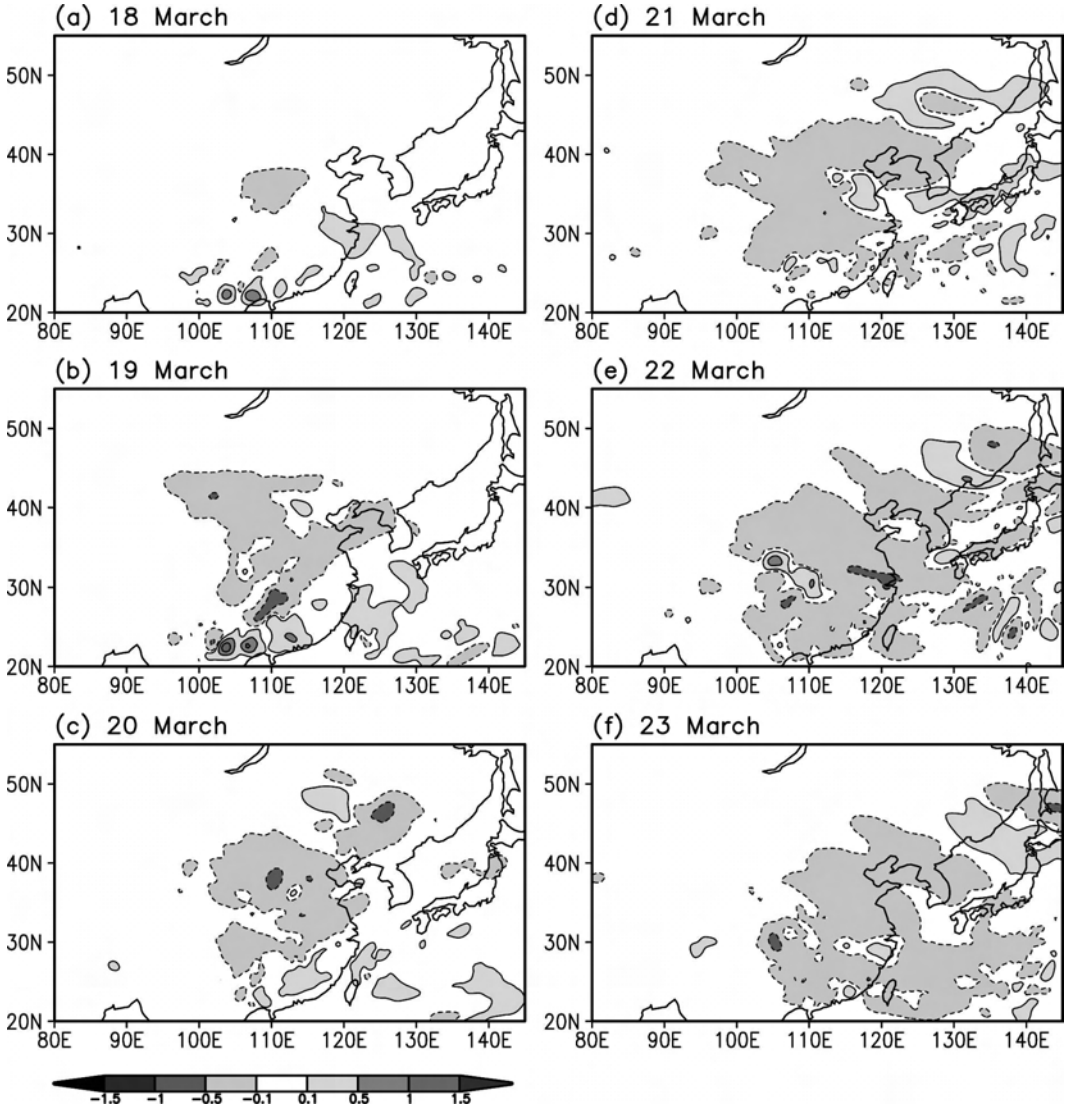

FIG. 14. As in Fig. 13, but at the 850-hPa level.

northeastern China and to the south of it as northwesterlies over central eastern China on 21 March (Fig. 16d).

Wind speed is an important parameter for the dust aerosol emission in the source region and transport of the aerosol in the upper level. Figures 17 and 18 show the daily mean wind speed difference change due to the perturbed circulation in association with the direct radiative effect of the aerosol at the surface and $\sigma = 0.45$ ($\cong$500 hPa) level, respectively. The difference of the wind speed is obtained by subtracting the wind speed simulated by the noncoupled model from that simulated by the coupled model.

The Asian dust aerosol is mainly emitted in the strong westerly or northwesterly wind region in northern China and Mongolia in the low level (Fig. 5); the easterly or southerly component of the perturbed circulation induced by the aerosol in the lower level reduces the low-level wind speed whereas the induced westerly or northerly component enhances the wind speed, resulting in the change of emission amount in the source region. In fact, in the surface layer (Fig. 17) the induced circulation reduces the wind speed over the maximum dust concentration region (Fig. 7) thereby reducing the emission amount whereas it enhances the wind in the downstream region of the maximum dust concentration, resulting in enhanced dust emission over the source region (Fig. 6). However, maximum wind speed change is about 1 m s^{-1} with a typical value of 0.25 m s^{-1} in the source region so that the enhanced emission amount in the source region is small as in Fig. 6.

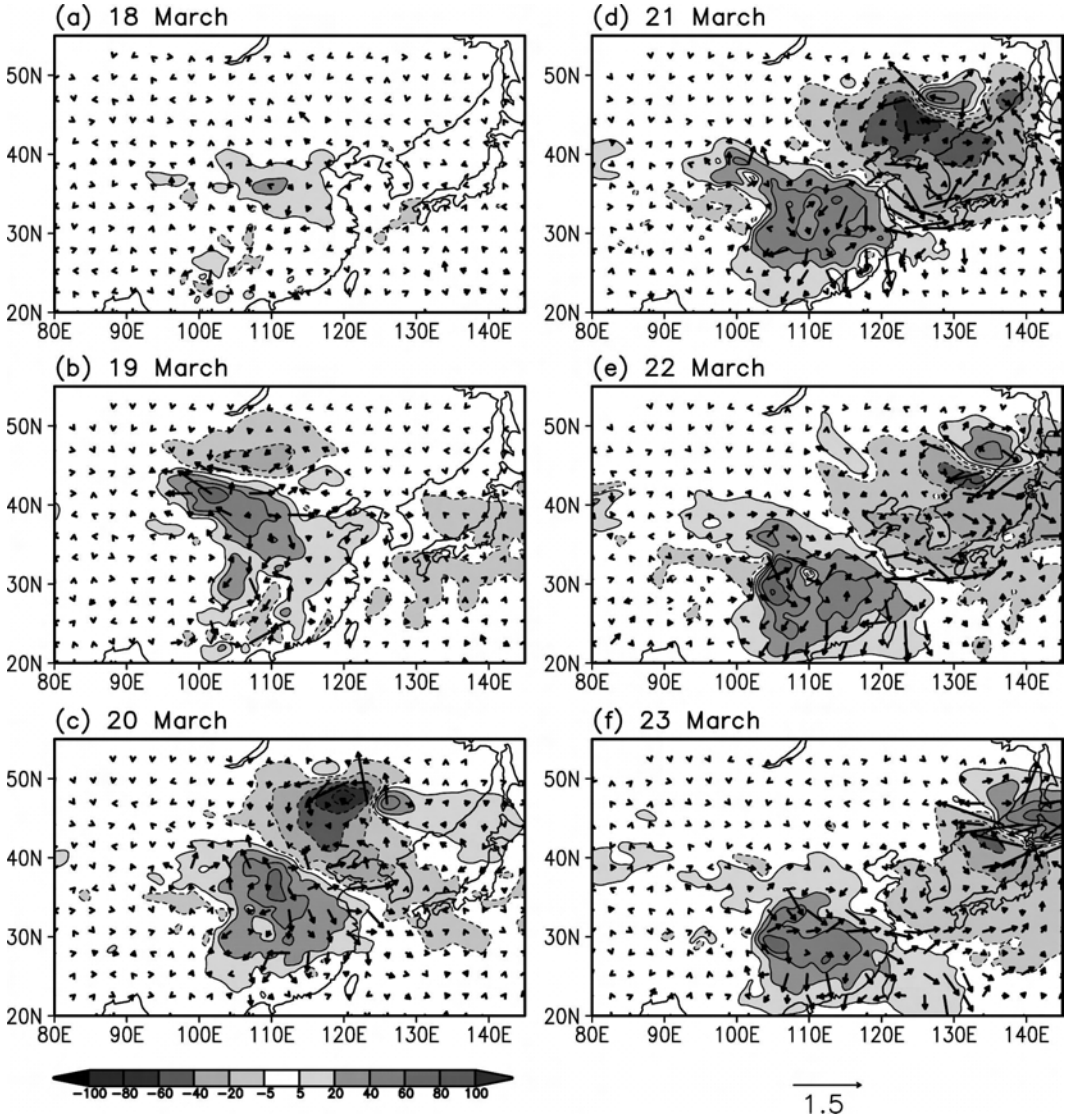

FIG. 15. As in Fig. 13, but for the pressure difference ($\times 10^{-2}$ hPa) and the wind vector difference (m s^{-1}).

On the other hand, in the upper level (Fig. 18) the enhanced wind speed transports the dust aerosol more quickly to the downstream region. The wind speed enhancement due to the aerosol effect mainly occurs over the maximum column-integrated dust concentration region (Fig. 8), so that the aerosol layer at that level (not shown) is elongated along the enhanced wind speed region (Fig. 18).

4) INTERNAL MODEL VARIABILITY

The forced response of the Asian dust aerosol on temperature (Fig. 13), pressure (Fig. 15), and wind (Fig. 17) fields can be distinguished from internal model variability if we know the spatial distribution of the internal model variability. For this purpose we have performed 10 simulations of 9 days from 16 to 24 March 2002 each with randomly perturbed initial meteorological fields using the unforced meteorological model.

The initial meteorological fields including temperature, pressure, u and v component of winds, and mixing ratio at each level are perturbed by giving a randomly generated maximum error of 3% of each variable at each grid point. The daily mean error of each variable averaged in the whole analysis domain is computed for each simulation and compared with the result of each simulation. The result indicates that the random error imposed in the initial field is slowly damped and oscillated with time. However, the different initial condition

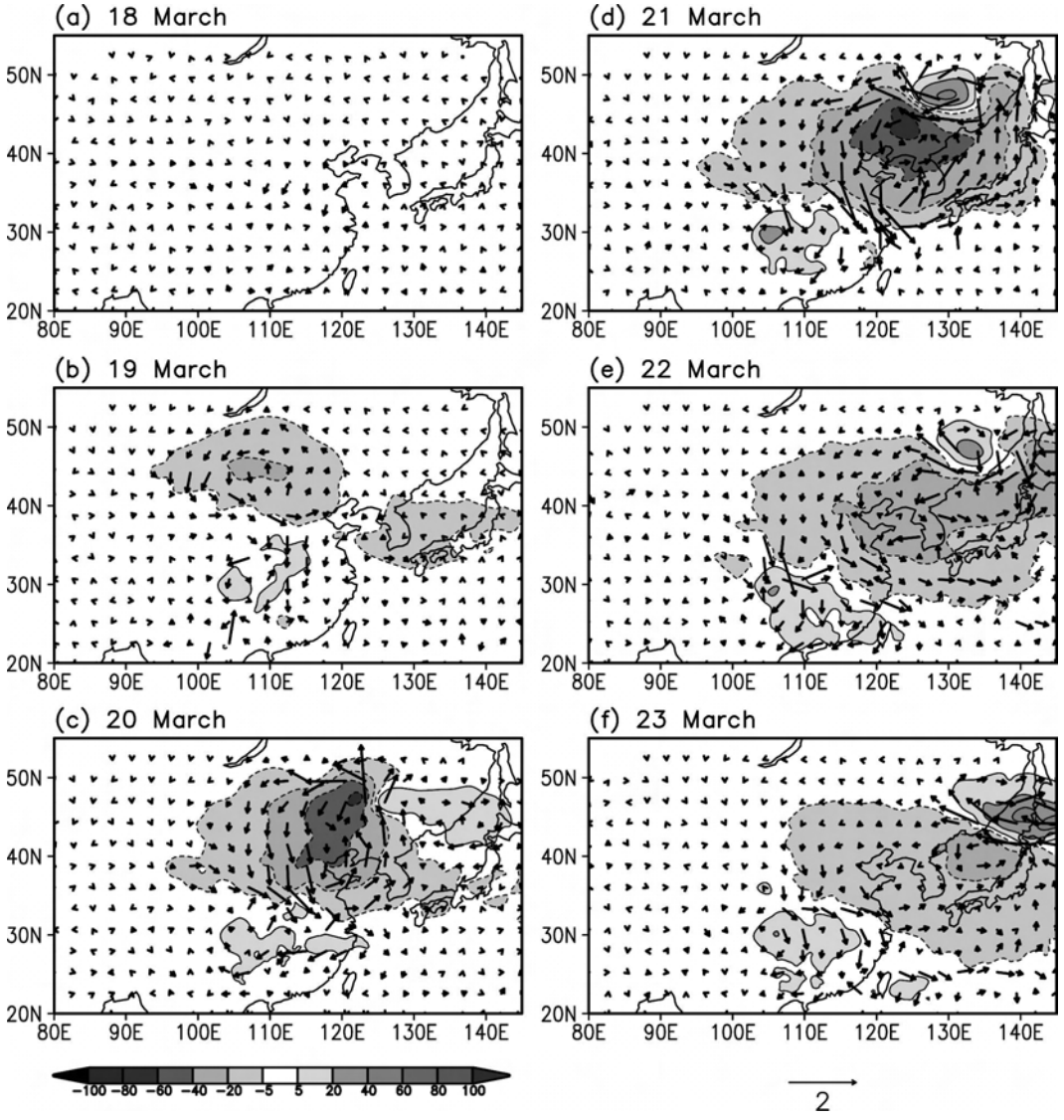

FIG. 16. As in Fig. 15, but at the 850-hPa level.

does not change the mean error of the domain. Thus we have performed 10 simulations of 9 days each with different initial conditions. The horizontal distribution of the standard deviations of temperature, pressure, and wind speed for 10 simulations near the surface is calculated and is given in Figs. 19–21.

Figure 19 shows that the temperature anomalies produced by the Asian dust radiative forcing (Fig. 19a) are much larger than the standard deviations of temperature induced by the internal model variability (Fig. 19b). The region of the large temperature anomaly induced by the aerosol radiative forcing does not coincide with that of the large standard deviation of temperature induced by internal model variability. The aerosol-induced temperature anomaly with the maximum value exceeding 1.5°C occurs in the high-dust-concentration region (Fig. 7), and the temperature change due to the internal model variability with the maximum value of less than 0.5°C tends to occur in the lower latitude (Fig. 19b), suggesting the presently estimated temperature anomaly in Fig. 13 is caused by the direct radiative forcing of the Asian dust.

Figure 20 shows the horizontal distribution of the pressure anomaly induced by the Asian dust radiative forcing (Fig. 20a) and the standard deviation induced by the internal model variability (Fig. 20b). It is clear that the pressure anomaly induced by the aerosol radiative forcing is larger than the standard deviation of pressure induced by the internal model variability. The maximum surface pressure anomaly induced by the

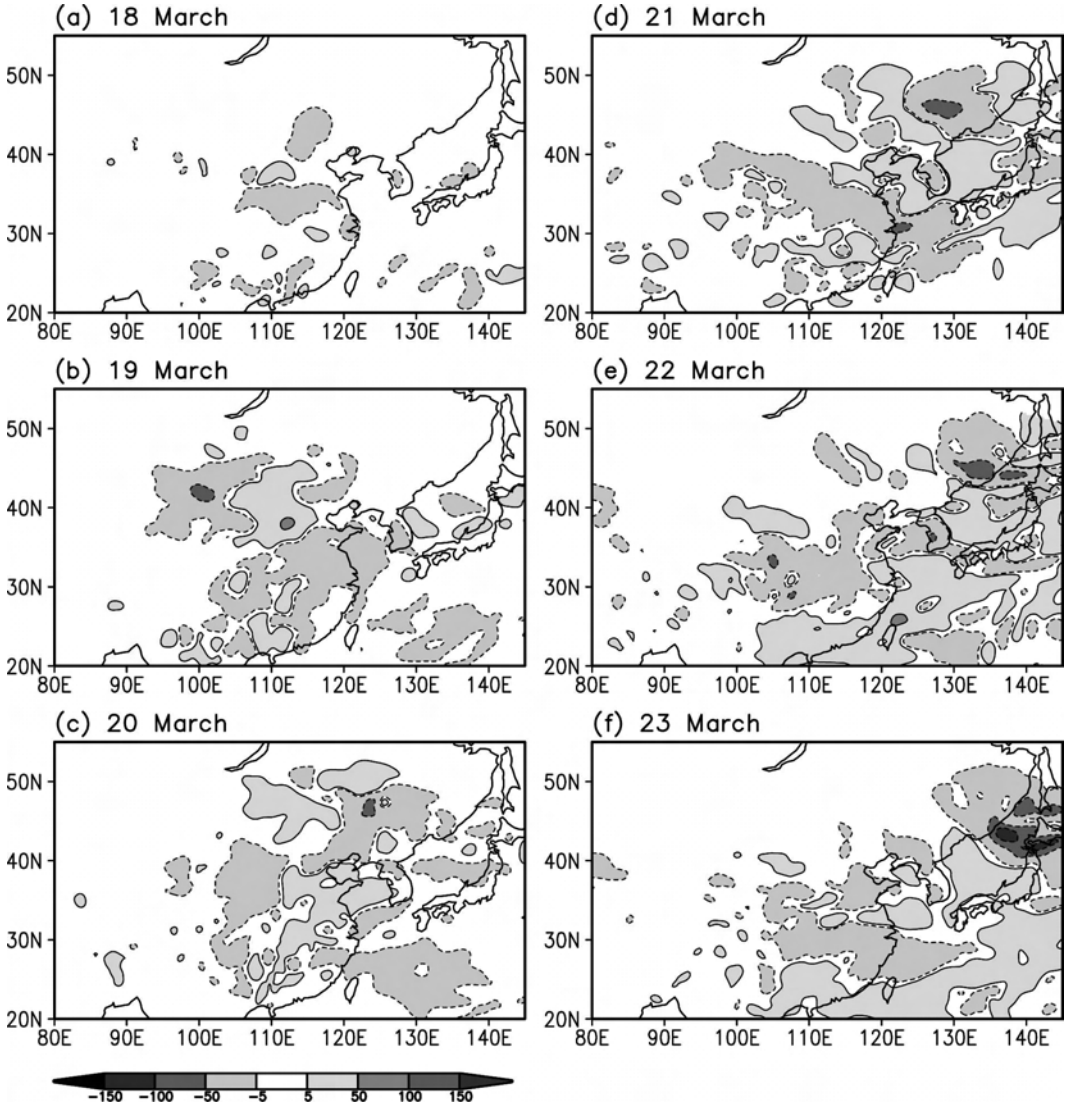

FIG. 17. As in Fig. 15, but for the wind speed difference (cm s^{-1}).

aerosol exceeds 0.6 hPa while the maximum standard deviation induced by the model variability is less than 0.2 hPa.

Note that the high internal model variability occurs in the synoptic low pressure system with the surface frontal system (Fig. 3). However, the internal model variability in the pressure field is much smaller than the pressure perturbation induced by the aerosol radiative forcing.

Figure 21 compares the horizontal distribution of the wind speed change induced by the aerosol radiative forcing (Fig. 21a) with that caused by the internal model variability (Fig. 21b). The occurrence region of the wind speed anomaly induced by the aerosol radiative forcing is different from that caused by the internal model variability. The maximum magnitude of the wind speed change of more than 1 m s^{-1} induced by the aerosol forcing is larger than that induced by the internal model variability that has a maximum value of 0.3 m s^{-1}. The horizontal distribution pattern of the standard deviation of the wind speed of the internal model variability (Fig. 21b) is very similar to that of temperature (Fig. 19b).

e. Vertical structure of the secondary circulation induced by the direct radiative forcing of the Asian dust aerosol

Vertical cross sections are constructed along the 36°N latitudinal band from 95° to 145°E on 21 March when the vertical integrated dust concentration is maxi-

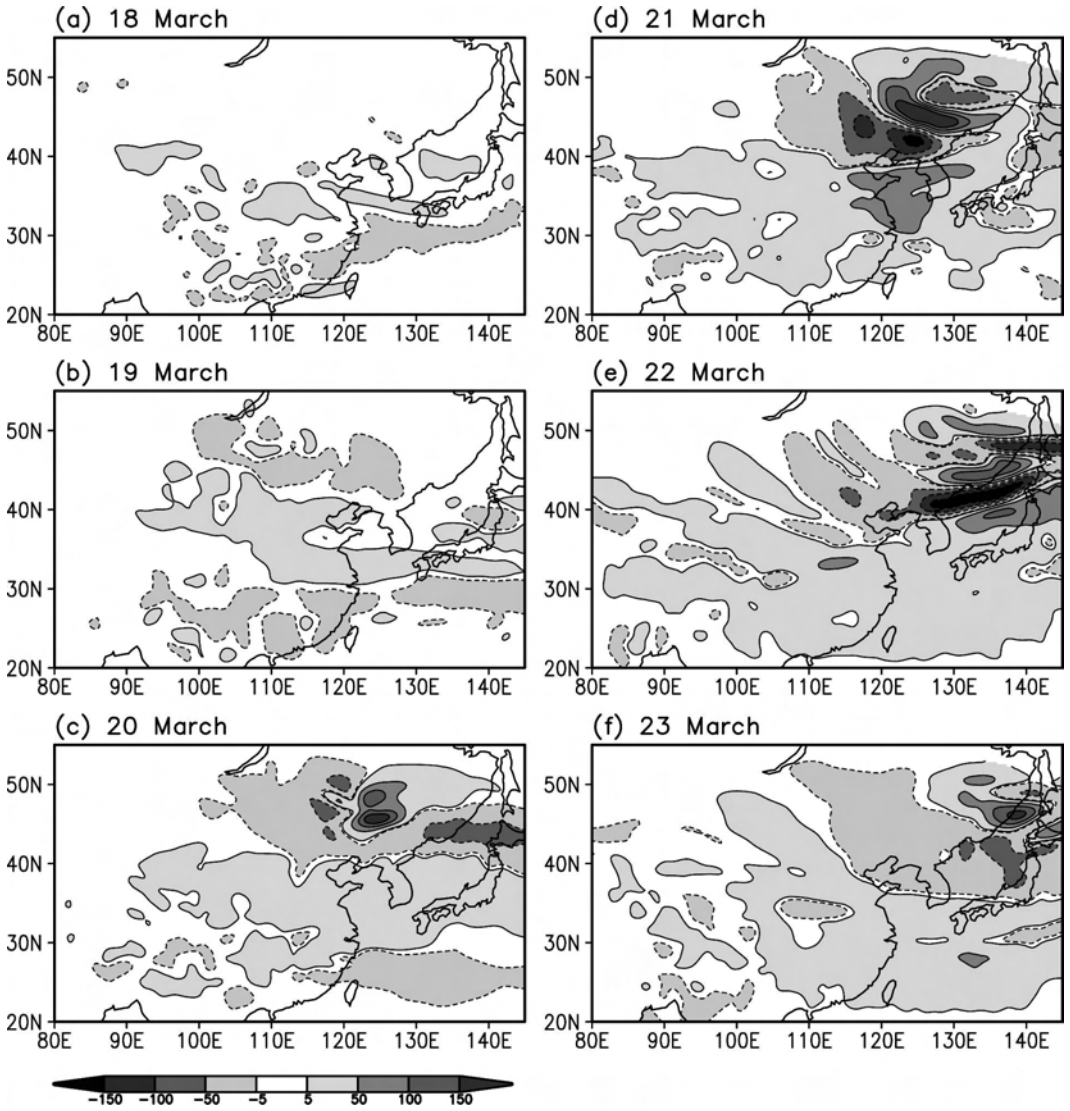

FIG. 18. As in Fig. 17, but at the 500-hPa level.

mum (Fig. 8). Figure 22 shows the vertical cross section of daily averaged mean fields simulated by the coupled model. The Asian dust has risen in the strong low-level westerly wind in the elevated source region (elevation of 2 km) at around 36°N, 105°E and has transported upward up to $\sigma = 0.45$ (about 500 hPa) as a result of the synoptic rising motion. The upward transported dust near the source area is quickly advected downstream along the strong upper-level environmental winds, whereas the relatively low-level weak wind advects the low-level high dust concentration extending from the surface more slowly, forming a bent-over plume shape. The plume shape is further modified by the mean vertical wind with the low-level confinement of high dust concentration in the sinking motion region and the vertical extension of high dust concentration in the rising-motion region.

The associated circulation induced by the direct radiative forcing of the Asian dust aerosol on 21 March is given in Fig. 23. The surface radiative cooling due to the Asian dust aerosol in the high-dust-concentration region induces sinking motion and a positive pressure perturbation that are mainly confined in the lower layer near the ground surface. The air layer at around 850 hPa between the upper-level overhanged dust layer and the low-level high dust layer is warmed because of the flux convergence. This warm air is advected downstream by the enhanced westerlies, reaching farther downstream in a wide range. Above the low-level positive pressure perturbation in the high-dust-concentra-

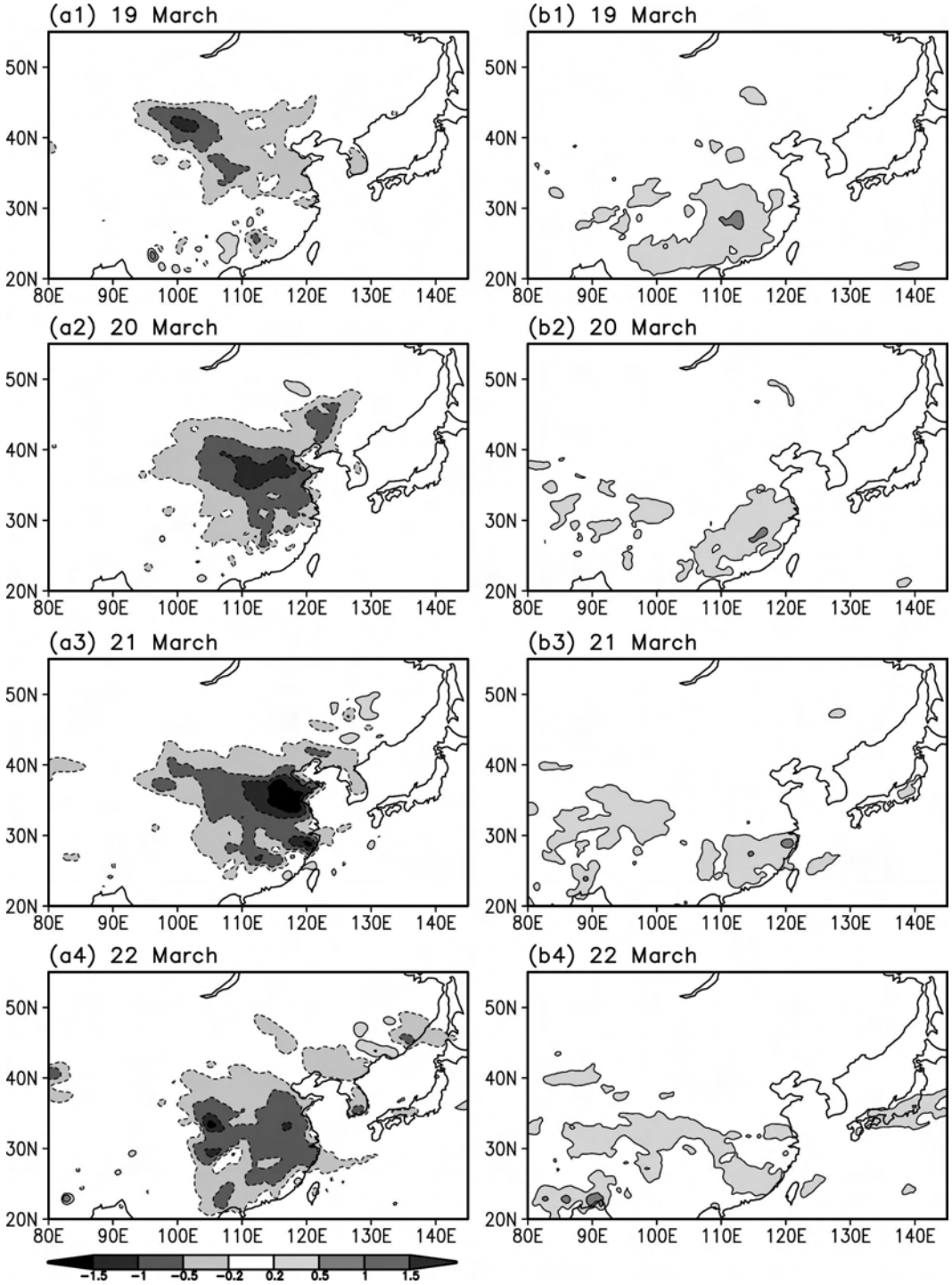

FIG. 19. Spatial distributions of temperature anomalies (°C) (a) forced by the Asian dust aerosol and (b) induced by internal model variability expressed by the standard deviation of temperature from 19 to 22 Mar 2002 at σ = 0.9975. The positive and negative values are respectively enclosed by the solid and dashed curves.

tion region, a very deep negative pressure-perturbation layer enhanced by the radiative cooling of the upper-level aerosol is formed and extends farther downstream, enhancing the induced circulation in a deep and wide region from the maximum-dust-concentration region. The effect of the direct radiative forcing of the dust aerosol on the wind field is consequently felt in the much deeper and wider downstream regions from the

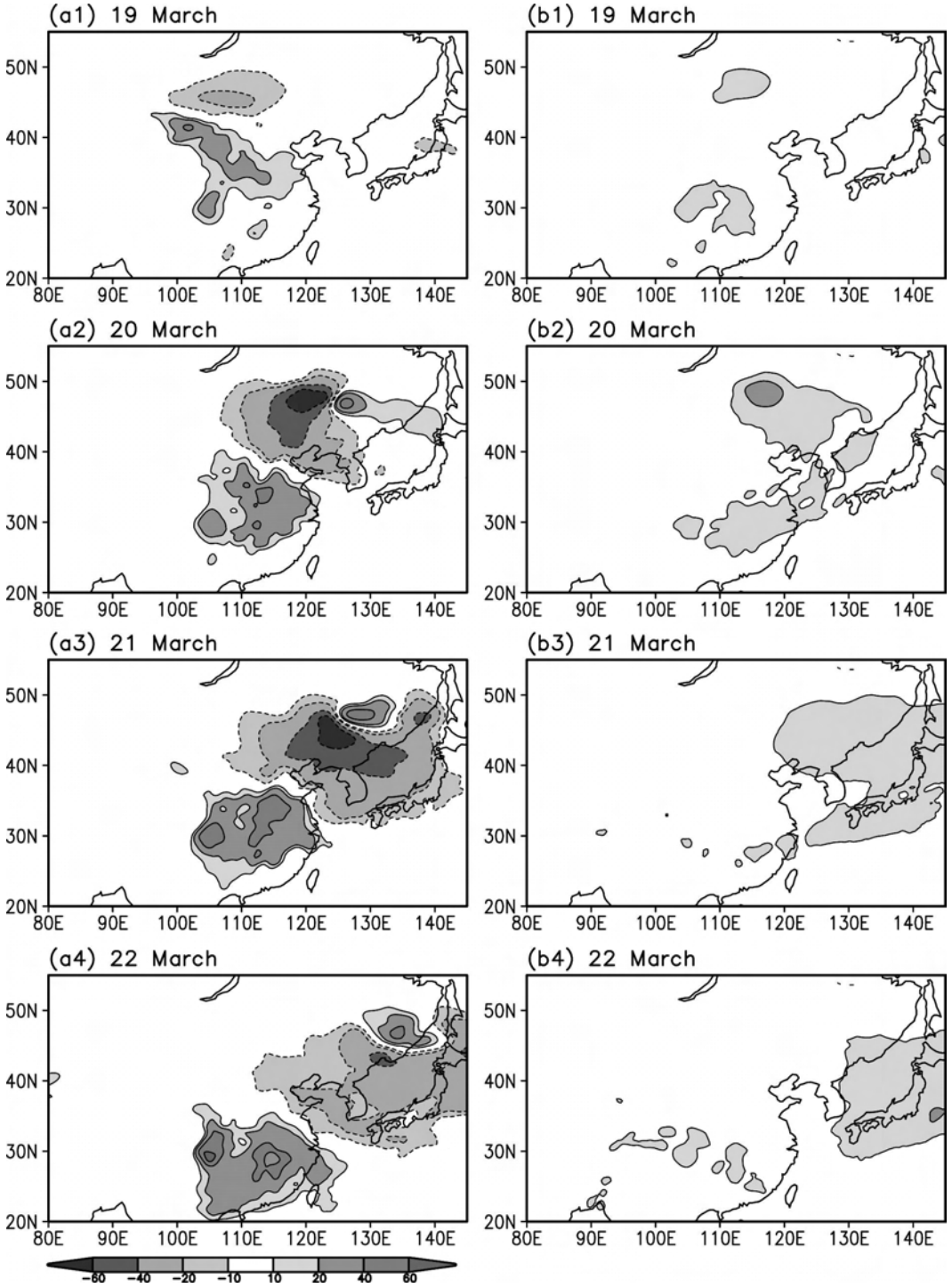

FIG. 20. As in Fig. 19, but for the pressure ($\times 10^{-2}$ hPa).

maximum-dust-concentration region through the pressure perturbation. The low-level cooling and upper-level warming induced by the dust enhance the stable stratification, which in turn reduces the cloud amount above the warm layer. This also affects the radiation balance in that layer. Even though the direct radiative cooling of the dust aerosol is not large (low-level temperature decrease of less than 2°C in the maximum-dust-concentration region), this cooling produces sinking motion near the surface and thereby positive pres-

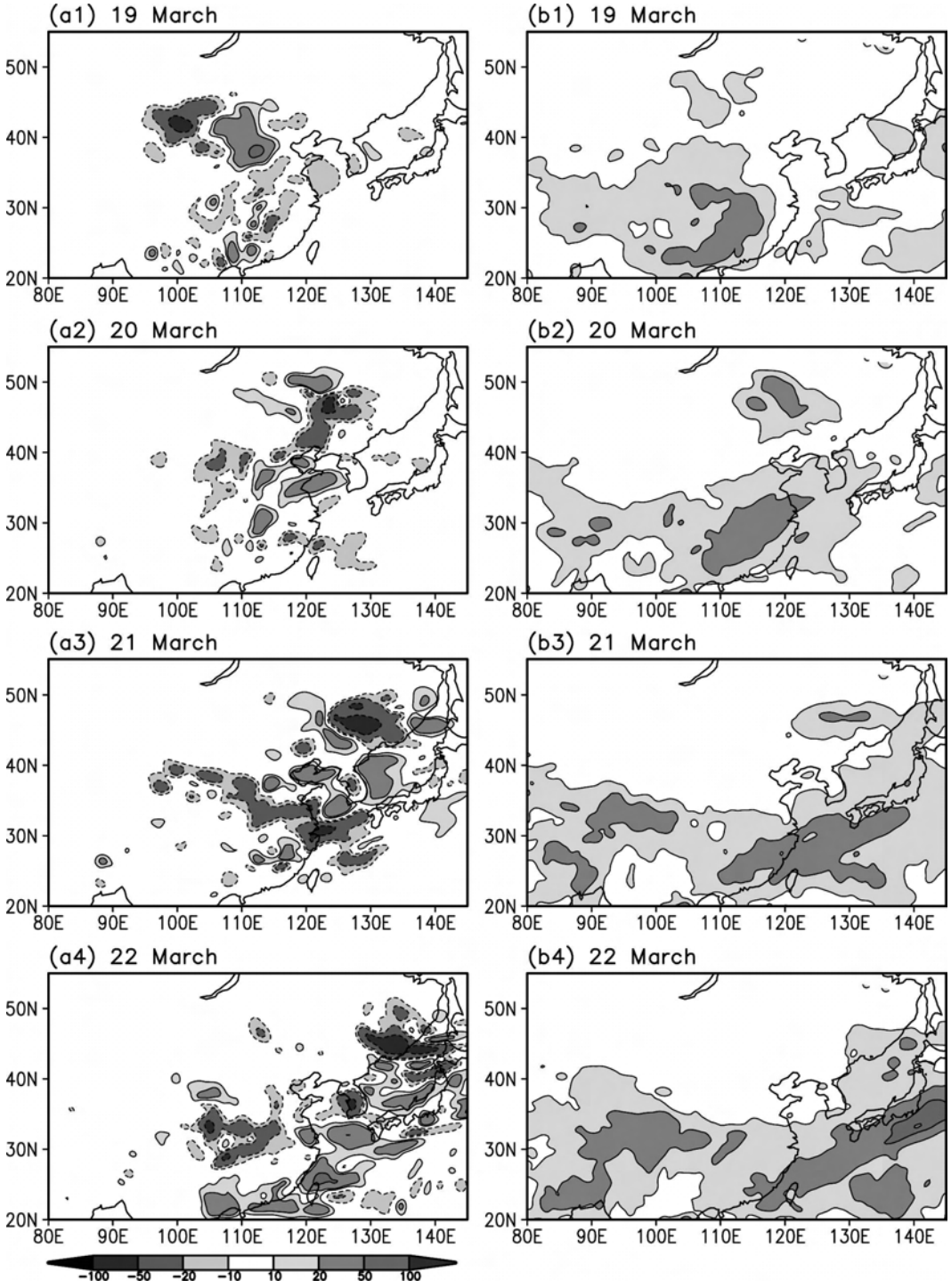

FIG. 21. As in Fig. 19, but for the wind speed (cm s^{-1}).

sure perturbation near the surface. In response to this, a negative pressure perturbation is enhanced in the deep layer and the wide downstream region, forming a dipole structure of pressure perturbation near the surface with a positive pressure perturbation in the maximum-concentration region and a negative pressure perturbation in the downstream direction. This pressure-perturbation field enhances the associated circulation in the wide downstream region, affecting meteorological fields in a wide downstream region.

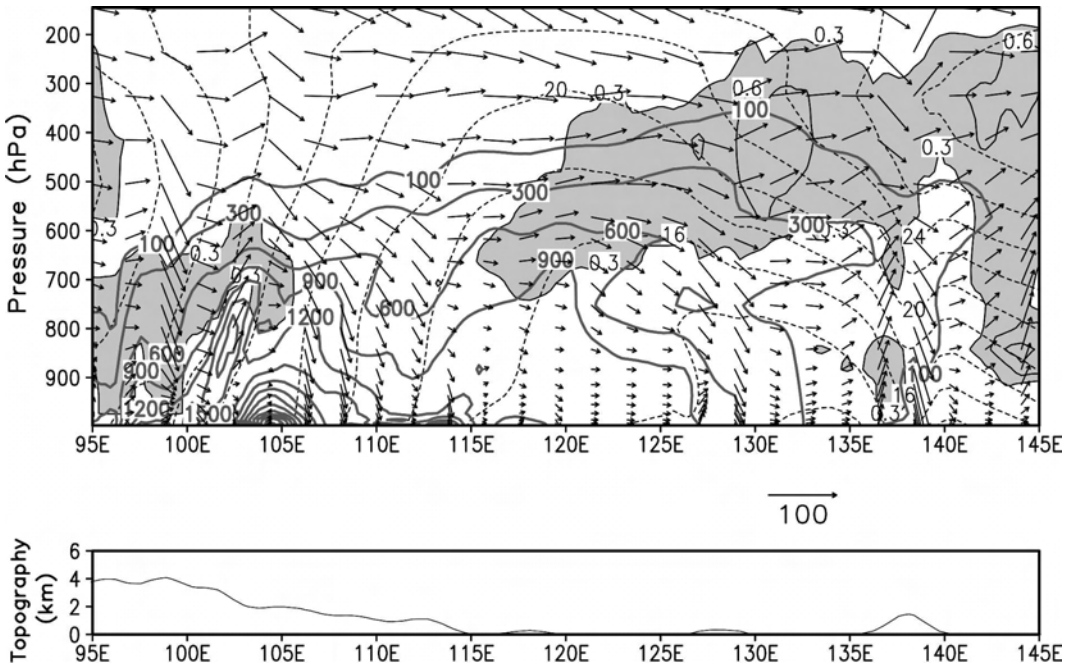

FIG. 22. (top) The vertical cross section of the mean U (m s^{-1})–W (10^{-3} m s^{-1}) vector wind (arrows), pressure perturbation (hPa; dashed lines), dust concentration (μg m^{-3}; thick lines) and cloud amount (shaded area) simulated by the coupled model constructed along 36°N from 95° to 145°E averaged on 21 Mar 2002. (bottom) The topographical height.

6. Summary and conclusions

The effects of direct radiative forcing due to the Asian dust aerosol on meteorological fields have been examined for an intense Asian dust event observed in eastern Asia on 18–23 March 2002 with the use of coupled and noncoupled models.

The coupled model consists of the modified MM5 that takes into account the direct radiative forcing of the Asian dust aerosol through the NCAR Column Radiation Model and the Asian Dust Aerosol Model, whereas the noncoupled model is MM5 without taking into account the direct radiative forcing of the dust. Both models have 120 × 65 grids in the eastern Asian domain with a horizontal grid spacing of 60 × 60 km^2 and 20 vertical levels in the σ coordinates. The difference between the meteorological fields simulated by the coupled model and the noncoupled model indicates the effect of the direct radiative forcing due to the Asian dust aerosol.

The results indicate that the radiative cooling at the surface due to the Asian dust aerosol over the high-dust-concentration region induces sinking motion and a positive pressure perturbation that are mainly confined near the surface. In response to this, a negative pressure perturbation is induced toward the low pressure center in the downstream region and the upper level, forming a dipole shape in the pressure-perturbation field near the surface with a positive pressure perturbation in the maximum-dust-concentration region and a negative pressure perturbation in the downstream region. The associated secondary circulation with these perturbed pressure fields causes the reduction of low-level wind speed upstream of the high-dust-concentration region (source region) where the induced wind direction is against the mean wind direction while strengthening the low-level wind speed in the downstream region where the induced wind direction is along the mean wind direction. This situation, in turn, reduces dust emission in the upstream source region, thereby reducing dust concentration because of the direct radiative forcing of the dust. The induced negative pressure perturbation is so deep and wide that the effect of radiative cooling of the dust aerosol from the source on the meteorological fields extends in the wide and deep regions. Some of the dust aerosols emitted in the source regions as a result of the low-level strong wind are lifted to a higher level in association with the synoptic rising motion and are transported to the downstream direction more quickly with the upper-level strong wind, causing a bent-over shape of the dust cloud in the downstream region, with a maximum concentration near the surface and a secondary maximum in the upper level. The layer between these two maximum con-

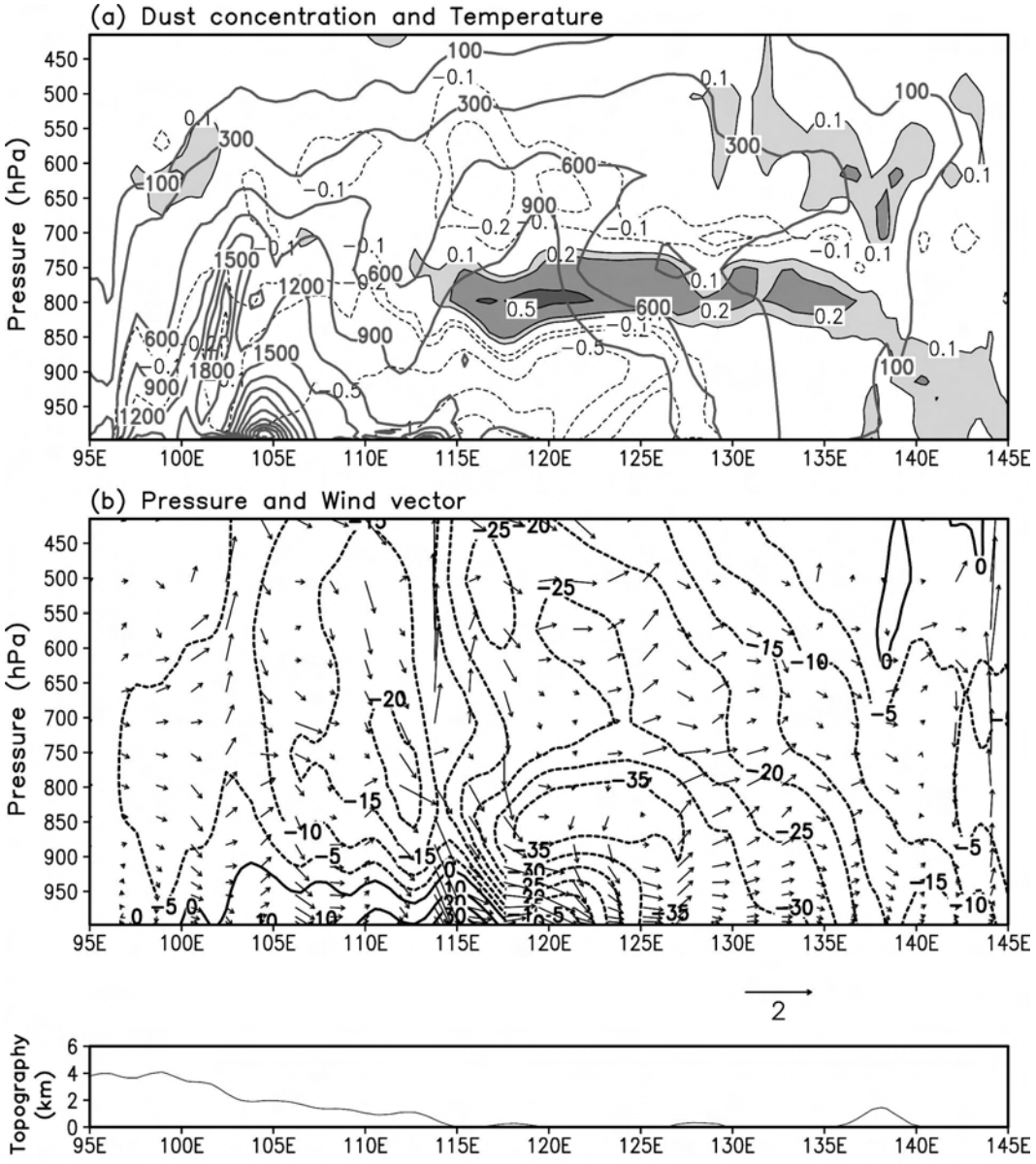

FIG. 23. As in Fig. 22, but for (a) mean dust concentration (μg m^{-3}; thick lines) and temperature difference (°C; the shaded area indicates positive values) and (b) pressure difference (10^{-2} hPa; solid lines are positive and dashed lines are negative) with U (m s^{-1})–W (2×10^{-2} m s^{-1}) vector wind difference (arrows).

centration layers is warmed as a result of radiative flux convergence, causing a warm layer. This warm air is advected to the downstream direction. The low-level cooling and upper-level warming induced by the dust aerosol enhance the stable stratification, which in turn, reduces the dust emission in the source region through the reduction of surface friction velocity and also cloud amount in the upper warm layer.

This study mainly pertains to estimating the effect of the direct radiative forcing of the Asian dust aerosol on the meteorological fields through the model results. However, the indirect effect of the dust aerosol on the meteorological fields is also known to be important. Further study on the direct and indirect effects of aerosols is a prerequisite to understanding climate change. Such study is now under way.

Acknowledgments. This research is partially supported by the Climate Environment System Research Center in Seoul National University and the Meteorol-

ogy and the Earthquake Research and Development program funded by the Korea Meteorological Administration. Special recognition is given to three anonymous reviewers for their helpful comments.

REFERENCES

Andreas, M. O., 1996: Raising dust in the greenhouse. *Nature,* **380,** 389–390.

Bott, A., 1989: A positive definite advection scheme obtained by nonlinear normalization of the advective fluxes. *Mon. Wea. Rev.,* **117,** 1006–1015.

Briegleb, B. P., 1992: Delta-Eddington approximation for solar radiation in the NCAR Community Climate Model. *J. Geophys. Res.,* **97,** 7603–7612.

Businger, J. A., J. C. Wyngaard, Y. Izumi, and E. F. Bradley, 1971: Flux profile relationships in the atmospheric surface layer. *J. Atmos. Sci.,* **28,** 181–189.

Chang, L.-S., 2005: Aerosol direct radiative forcing in east Asia. Ph.D. dissertation, Seoul National University, 30 pp.

Chatenet, B., B. Marticorena, L. Gomes, and G. Bergametti, 1996: Assessing the micro size distribution of desert soils erodible by wind. *Sedimentology,* **43,** 901–911.

Chun, Y., K.-O. Boo, J. Kim, S.-U. Park, and M. Lee, 2001: Synopsis, transport, and physical characteristics of Asian dust in Korea. *J. Geophys. Res.,* **106,** 18 461–18 469.

Chung, K. Y., and S.-U. Park, 1995: Characteristic synoptic features associated with the transport of yellow sand to Korea. *Korean J. Atmos. Sci.,* **31,** 45–63.

Chung, Y.-S., and T.-K. Kim, 1991: A study on long range transport of air pollutants-sources and observations of yellow sand, TSP and sulphate in Korea (in Korean). *J. Korean Soc. Atmos. Environ.,* **7,** 197–202.

Dudhia, J., D. Grill, Y.-R. Guo, D. Hausen, K. Manning, and W. Wang, 1998: PSU/NCAR mesoscale modeling system tutorial class notes (MM5 modeling system version 2).

Giorgi, F., 1986: A particle dry-deposition parameterization scheme for use in tracer transport models. *J. Geophys. Res.,* **91,** 9794–9806.

Gomes, L., G. Bergametti, F. Dulac, and U. Ezat, 1990: Assessing the actual size distribution of atmospheric aerosols collected with a cascade impactor. *J. Aerosol Sci.,* **21,** 47–59.

Grell, G. A., J. Dudhia, and D. R. Stauffer, 1994: A description of the fifth-generation Penn State/NCAR Mesoscale Model (MM5). NCAR Tech. Note NCAR/TN-398, 117 pp.

Husar, R. B., and Coauthors, 2001: Asian dust events of April 1998. *J. Geophys. Res.,* **106,** 18 317–18 330.

In, H.-J., and S.-U. Park, 2002: A simulation of long-range transport of Yellow Sand observed in April 1998 in Korea. *Atmos. Environ.,* **36,** 4173–4187.

——, and ——, 2003: The soil particle size dependent emission parameterization for an Asian dust (Yellow Sand) observed in Korea in April 2002. *Atmos. Environ.,* **37,** 4625–4636.

——, E.-H. Lee, and S.-U. Park, 2003: Estimation of dust deposition for the Yellow Sand event observed in April 1998 in Korea. *Korean J. Atmos. Sci.,* **6,** 13–25.

Joseph, J. H., J. W. Wiscombe, and J. A. Weinman, 1976: The delta-Eddington approximation for radiative flux transfer. *J. Atmos. Sci.,* **33,** 2452–2459.

Kiehl, J. T., J. J. Hack, G. B. Bonan, B. A. Boville, D. L. Williamson, and P. J. Rasch, 1998: The National Center for Atmospheric Research Community Climate Model: CCM3 *J. Climate,* **11,** 1131–1149.

Li, X., H. Maring, D. Savoie, K. Voss, and J. M. Prospero, 1996: Dominance of mineral dust in aerosol light scattering in the North Atlantic trade winds. *Nature,* **380,** 416–419.

Lu, H., and Y. Shao, 1999: A new model for dust emission by saltation bombardment. *J. Geophys. Res.,* **104,** 16 827–16 842.

Miller, R. L., and I. Tegen, 1998: Climate response to soil dust aerosols. *J. Climate,* **11,** 3247–3267.

——, J. Perlwitz, and I. Tegen, 2004: Feedback upon dust emission by dust radiative forcing through the planetary boundary layer. *J. Geophys. Res.,* **109,** D24209, doi:10.1029/2004JD004912.

Park, S.-U., 2002: Field survey of yellow sand source regions. *Proc. Workshop of Asian Dust,* Seoul, South Korea, Korea Meteorological Administration, 13–47.

——, and H.-J. In, 2003: Parameterization of dust emission for the simulation of the Yellow Sand (Asian dust) observed in March 2002 in Korea. *J. Geophys. Res.,* **108,** 4618, doi:10.1029/2003JD003484.

——, and E.-H. Lee, 2004: Parameterization of Asian dust (Hwangsa) particle-size distributions for use in dust emission model. *Atmos. Environ.,* **38,** 2155–2162.

——, L.-S. Chang, and E.-H. Lee, 2005: Direct radiative forcing due to aerosols in east Asia during a *Hwangsa* (Asian dust) event observed on 19–23 March 2002 in Korea. *Atmos. Environ.,* **39,** 2593–2606.

Perlwitz, J., I. Tegen, and R. L. Miller, 2001: Interactive soil dust aerosol model in the GISS GCM 1. Sensitivity of the soil dust cycle to radiative properties of soil dust aerosols. *J. Geophys. Res.,* **106,** 18 167–18 192.

Prospero, J. M., D. L. Savoie, T. N. Carlson, and R. T. Nees, 1979: Monitoring Saharan aerosol transport by means of atmospheric turbidity measurements. *Saharan Dust: Mobilization, Transport, Deposition,* C. Morales, Ed., John Wiley and Sons, 171–191.

Schultz, L., 1979: Saharan dust transport over the North Atlantic Ocean Model calculation and measurements in Saharan Desert. *Saharan Dust: Mobilization, Transport, Deposition,* C. Morales, Ed., John Wiley and Sons, 267–277.

Seinfeld, J. H., and S. N. Pandis, 1998: *Atmospheric Chemistry and Physics*. John Wiley and Sons, 1360 pp.

Shao, Y., 2001: A model of mineral dust emission. *J. Geophys. Res.,* **106,** 20 239–20 254.

——, E. Jung, and L. M. Leslie, 2002: Numerical prediction of northeast Asian dust storms using an integrated wind erosion modeling system. *J. Geophys. Res.,* **107,** 4814, doi:10.1029/2001JD001493.

Tegen, I., and I. Y. Fung, 1994: Modeling of mineral dust in the atmosphere: Sources, transport, and optical thickness. *J. Geophys. Res.,* **99,** 22 897–22 914.

——, and ——, 1995: Contribution to the atmospheric mineral aerosol load from land surface modification. *J. Geophys. Res.,* **100,** 18 707–18 726.

——, A. A. Lacis, and I. Y. Fung, 1996: The influence on climate forcing of mineral aerosols from disturbed soils on global radiation budget. *Nature,* **380,** 419–422.

Wesely, M. L., 1989: Parameterization of surface resistance to gaseous dry deposition in regional-scale numerical models. *Atmos. Environ.,* **23,** 1293–1304.

Westphal, D. L., O. B. Toon, and T. N. Carlson, 1987: A two dimensional investigation of the dynamics and microphysics of Saharan dust storms. *J. Geophys. Res.,* **92,** 3027–3049.

——, ——, and ——, 1988: A case study of mobilization and transport of Saharan dust. *J. Atmos. Sci.,* **45,** 2145–2175.